DALHOUSIE UNIVERSITY

TESTING A MUOGENIC ISOTOPE METHOD TO MONITOR RELIEF GENERATION OVER MILLIONS OF YEARS

Maya Soukup

SUBMITTED IN PARTIAL FULFILLMENT OF THE REQUIREMENTS FOR THE DEGREE
OF BACHELOR OF SCIENCES, HONOURS
DEPARTMENT OF EARTH SCIENCES
DALHOUSIE UNIVERSITY,HALIFAX, NOVA SCOTIA

April 2018

Distribution License

DalSpace requires agreement to this non-exclusive distribution license before your item can appear on DalSpace.

NON-EXCLUSIVE DISTRIBUTION LICENSE

You (the author(s) or copyright owner) grant to Dalhousie University the non-exclusive right to reproduce and distribute your submission worldwide in any medium.

You agree that Dalhousie University may, without changing the content, reformat the submission for the purpose of preservation.

You also agree that Dalhousie University may keep more than one copy of this submission for purposes of security, back-up and preservation.

You agree that the submission is your original work, and that you have the right to grant the rights contained in this license. You also agree that your submission does not, to the best of your knowledge, infringe upon anyone's copyright.

If the submission contains material for which you do not hold copyright, you agree that you have obtained the unrestricted permission of the copyright owner to grant Dalhousie University the rights required by this license, and that such third-party owned material is clearly identified and acknowledged within the text or content of the submission.

If the submission is based upon work that has been sponsored or supported by an agency or organization other than Dalhousie University, you assert that you have fulfilled any right of review or other obligations required by such contract or agreement.

Dalhousie University will clearly identify your name(s) as the author(s) or owner(s) of the submission, and will not make any alteration to the content of the files that you have submitted.

If you have questions regarding this license please contact the repository manager at dalspace@dal.ca.

Grant the distribution license by signing and dating below.

_____ _____

Name of signatory Date

Department of Earth Sciences
Halifax, Nova Scotia
Canada B3H 4R2
(902) – 494 – 2358

AUTHOR: Maya A. Soukup

TITLE: Testing a muogenic isotope method to monitor relief generation over millions of years

DEGREE: BSc. Earth Science (Honours, Co-op) CONVOCATION: Spring YEAR: 2018

ABSTRACT

Terrestrial Cosmogenic Nuclide (TCN) methods have been traditionally focused on the measurement of radionuclides in the top 4 m of the lithosphere down to where calibrated data exists at depths of <30 m. Improvements in TCN target chemistry and Accelerator Mass Spectrometry have provided an opportunity to expand this depth in an effort to address previously intractable questions regarding topographic evolution. The primary objective of this thesis is to test the validity and reproducibility of measuring a long-lived TCN (^{10}Be, t½= 1.39 Ma) using muon-produced nuclides at great depths. The secondary objective of this thesis involves applying this method to study the history of incision and large scale relief generation. The test site for the application is a small valley near the Book Cliffs, Utah. The results of AMS measurements on 6 BeO targets prepared from deeply shielded quartzite suggest that muogenic ^{10}Be can be measured with sufficient precision at depths exceeding 100 m to establish when a valley may have evolved over million-year timescales.

Keywords: Muon, TCN, ^{10}Be, topography, incision

TABLE OF CONTENTS

LIST OF TABLES

TABLE OF FIGURES

LIST OF ABBREVIATIONS

- Galactic Cosmic Radiation (GCR)
- Terrestrial in situ Cosmogenic Nuclides (TCN)
- Cosmic Rays (CR)
- Optically Stimulated Luminescence (OSL)
- Thousand years (ka)
- Million years (Ma)

ACKNOWLEDGMENTS

I would like to acknowledge first and foremost my supervisor Dr. John Gosse for giving me the opportunity to conduct this research, and for creating an environment where I could learn and challenge myself. I would also like to thank Dr. Alan J. Hidy for giving me the chance to see the AMS run at Lawrence Livermore National Laboratory firsthand, as well as temporarily oversee and monitor its operations. I would like to thank Dr. Joel L. Pederson for his invaluable contribution to the geomorphological understanding of the Colorado River's history of incision, and for his involvement in this collaboration. Additionally, I would like to thank Guang Yang for teaching me complex, high precision analytical chemistry, and to allow me to conduct much of the sample preparation under her guidance. Finally, I would like to thank everyone in the CRISDal Laboratory for their endless support and encouragement.

1 INTRODUCTION

The desire to know when and how landscapes have evolved is a fundamental pursuit rooted in the primordial human need to explore its environment, understand geohazards, and relate to their place on the Earth's surface. Presently, many techniques have been employed to provide some constraints on the development of topography. These techniques include mapping of strath and fill terraces and cross cutting relationships, geochronology of those terraces, thermochronology methods that attempt to reveal different cooling histories of rocks in the valleys and surrounding interfluves, long-term incision rates inferred from paleo-erosion rates or paleo-sediment flux methods, and exposure dating of fluvially scoured surfaces on steep-walled canyons (Staiger et al. 2007, Pederson et al. 2013b, 2013c). However, there are limitations to all of these methods. For instance, terraces and fluvially-scoured canyon faces are ill-preserved beyond millions of years, incision history may be faster and shorter than can be evaluated by low-temperature thermochronometers that are limited to the upper few kilometres, and few chronometers that are reliable in the million-year time range are applicable (exceptions include $^{40}Ar/^{49}Ar$ or Terrestrial Cosmogenic Nuclide (TCN) exposure dating of lava that has fallen into a valley (Fenton et al. 2013)). Therefore, establishing another approach to quantify the rate and timing of incision would be immediately useful for research on large-scale surface processes and geodynamics research.

Improvements in sample preparation and measurement of TCN, and our understanding of TCN production pathways through different nuclear interactions has afforded an opportunity to explore a new approach to study large-scale incision history. Cosmic ray produced muons, created in Earth's atmosphere and lithosphere when primary cosmic ray protons interact with exposed atoms, can penetrate deeply into rock and produce TCN such as ^{10}Be and ^{26}Al, among others. This thesis is the first attempt to test the possibility that the spatial variation in concentrations of muogenic nuclides sampled along a subsurface horizontal cross-valley transect under a valley may provide a useful estimate of rate and timing of valley incision. The thesis first determines if muogenic ^{10}Be can be measured with sufficient precision to allow the discrimination of concentrations under a valley, and then attempts to interpret a dataset to evaluate the erosion history over hundreds of thousands to millions of years. The test area for the pilot study is a small tributary valley in the Book Cliffs, Utah.

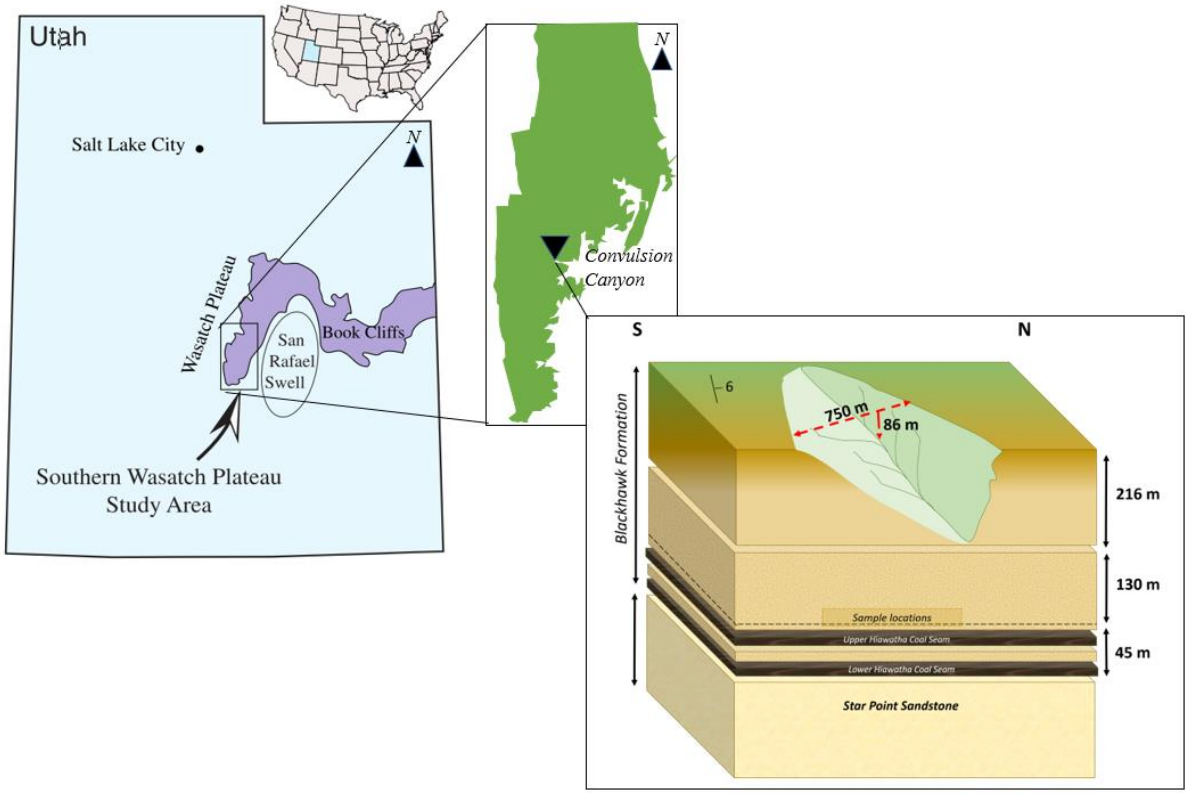

Figure 1-1. Figure of the location of our study area in central Utah. The diagram on the right depicts the cross section through the tributary where the mine stope is located, which was excavated to target the Upper Hiawatha Coal Seam, which has estimated reserves between 300 – 420 million short tonnes of coal (Modified from (Dubiel et al., (2000), inset stratigraphy by Soukup 2018).

The tributary valley incision is located on the northern edge of Convulsion Canyon, Sevier County, Utah. This incised valley is located on the southwestern portion of the Wasatch Plateau, which is the westernmost arm of the Book Cliffs (fig. 1-1). The SUFCO Mine operates out of this tributary incision targeting the Upper Hiawatha Coal Seam in the deep strata of the Upper Cretaceous Blackhawk Formation. The samples in this thesis were obtained from a lateral mine stope that runs roughly perpendicular to the axis of the valley above, at shielded depths between 130 and 216 m below the valley incision through the Lower Blackhawk Formation. This formation consists of interbedded deltaic sandstones and bituminous coal seams, the thickest of which are targeted for exploitation (Dubiel et al. 2000).

.

The precision of the measurements of muogenic ^{10}Be at depths greater than 200 m below ground, supports the possibility of a muogenic TCN approach for large-scale landscape evolution questions that require as little as 20% analytical precision. The results reveal that the ^{10}Be concentrations can be interpreted as erosion rates. In this experiment, the spatial pattern of the

^{10}Be concentrations along the sub-valley transect did not mimic the topography above, suggesting either that the test valley was incised very recently, or other factors, such as low-angle cosmic ray flux penetrating through the Book Cliffs, play a significant role. The test results are therefore important because they demonstrate the plausibility of a new approach to landscape evolution, and will guide refinement of the procedures to apply the method.

2 BACKGROUND

The focus of this thesis is on the ^{10}Be nuclide produced from interaction with fast muons at depth to interpret geomorphological evolution. To understand this focus, knowledge of the behaviour of cosmogenic nuclides in the atmosphere and lithosphere is essential.

2.1 PRINCIPLES OF COSMIC RAYS

Galactic Cosmic Radiation (GCR) is the primary source of accelerated particles, consisting of mainly protons that penetrate the Earth's magnetic field to interact with matter in the Earth's atmosphere and lithosphere; the interaction of Cosmic Rays (CR) in the atmosphere and lithosphere occurs predominantly through a process referred to as spallation. Spallation is a two-step process in which the primary proton elastically collides with an atmospheric nucleus (e.g. ^{14}N or ^{16}O) by first breaking the nucleus into two or more pieces, and then the energy from the shock wave penetrating through those pieces further exceeds the binding energy of their nucleons, resulting in a shower of energetic secondary particles ranging from neutrons, muons, and other subatomic particles and electromagnetic radiation to larger particles such as ^{14}C. This cascade of secondary particles, referred to as a 'cosmic ray shower' continues to interact with matter in the atmosphere, hydrosphere, biosphere, and lithosphere through interactions including spallation, thermal neutron capture, and various muonic interactions. Even after an average of ten disintegrations through an atmospheric mass depth of 1000 g cm^{-2} (mass depth is a length quantity that is independent of density, meaning that mass depth is the product of depth (cm) and density (g cm^{-3})), the secondary radiation has sufficient energy to produce cosmogenic nuclides in the upper few hundred metres of Earth's lithosphere. Therefore, muons are secondary particles, derived from the muonic interaction with matter in the lithosphere (Gosse and Klein, 2015).

The large attenuation lengths of muons that allow for deeper penetration of muons at depth is one of the leading reasons for innovation towards utilizing muon-induced production at great depths. The *e-folding length* (the mass depth (g·cm^{-2}) over which the average energy o f the particle flux diminishes by a factor of 1/*e*) of muons is much longer than that of larger particles. The attenuation length of fast neutrons (Λ_{nf}) is 150-160 g·cm^{-2} (Gosse and Phillips, 2001), while comparatively, the attenuation length of slow negative muons ($\Lambda_{\mu s}$) is 1,500g·cm^{-2} (Heisinger et al. 2002a), and the attenuation length for fast muons ($\Lambda_{\mu f}$) is 4,320 g·cm^{-2} (Heisinger et al.

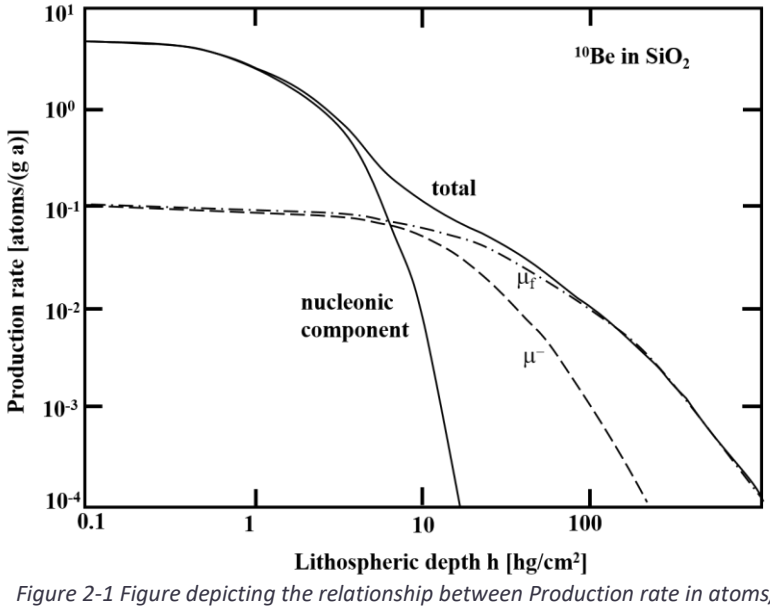

Figure 2-1 Figure depicting the relationship between Production rate in atoms/g-1yr-1 versus Lithospheric depth (hg/cm2). This figure shows that with increasing depth, the production mechanisms change from spallation to muonic production, meaning that muonic production of TCN occurs in higher proportion than nucleonic component production at depths greater than ~10hg/cm2 (from Heisinger et al., 2002a).

2002b). With a mass 90 times smaller than a proton, the muon interacts weakly with matter. Muons undergo a decrease in energy and flux with depth due to three processes; ionization, inelastic collisions, and by emitting a limited amount of *bremsstrahlung* (energy released in the form of gamma rays). Due to the negative charge of the slow muon, these particles interact more strongly with matter than fast muons, which are more energetic. This characteristic allows fast muons to penetrate to greater depths than other cosmic ray secondaries before interacting with matter. Currently, the ultimate depth of penetration through surfaces by muons is not known, but has been tested to depths of 49,300 g cm^{-2} (197 m) by Kim et al. (2004), where they achieved <7% uncertainty based on AMS counting statistics only. More information on the background of Terrestrial Cosmogenic Methods can be found in Appendix B.

2.2 APPROACHES TO RELIEF DEVELOPMENT OF THE COLORADO PLATEAU

Most incision rates across the Colorado Plateau have been measured from the Grand Canyon Province in the Southwest area of the plateau, and vary over the last 500 ka. Incision rates have been identified with different techniques including Uranium Series and Optically Stimulated Luminescence (OSL) (Pederson et al. 2013a), ^{40}Ar/^{49}Ar (Pederson et al. 2002a), Apatite Thermochronometry (Murray et al. 2016), and TCN Dating of strath and fill terraces (Wolkowinsky and Granger 2004, Cook et al. 2009).

Table 2-1 Table of incision rate estimates from the Colorado River and its tributaries over the last 500 kyr collected between 2001 and 200 (from Garvin et al., 2005).

Location	***Time Period (ka)***	***Incision rate (m ka^{-1})***	***Sources cited***
Colorado River; Grant Canyon Granite Park	500- present	0.072 – 0.092	Pederson et al., (2002)
Colorado River; Eastern Grand Canyon	500 – present	0.135 – 0.144	Pederson et al., (2002)
Colorado River; Grand Canyon, Granite Park	600 – present	0.09-0.16	Lucchitta et al., (2001)
Virgin River; Zion National Park	1060 – present	0.38	Willis and Biek (2001)
Colorado River; Glen Canyon, Bullfrog Basin	500 -present	0.4	Davis et al., (2000)
Colorado River; Lees Ferry	500 – present	0.31 – 0.48	Lucchitta et al., (2000)
Fremont River; Capitol Reef	190 – present	0.4	Marchetti and Cerling (2001)
Colorado River; Glen Canyon, Navajo Mt	500 – present	0.5	Hanks et al. (2001)
Colorado River; Glen Canyon, Navajo Mt	500 – 250	0.4	Garvin et al. (2005)
Colorado River; Glen Canyon, Navajo Mt	250 – present	0.7	Garvin et al. (2005)
Oak Creek & Bridge Creek; Navajo Mt	100 - present	0.6	Garvin et al. (2005)

Stratigraphic techniques have also been applied to understanding the erosional history of the Colorado River. The Miocene-aged Muddy Creek Formation is of special interest, and contains within it evidence of 10 Ma remnant lake beds that were filled prior to the incision of the Grand Canyon, and marks deposits indicative of the inception of Colorado River streamflow into the Gulf of California ~ 6 Ma (Faulds et al. 2001). At the top of the Muddy Creek Formation section as determined by Lucchitta et al. (1972), the Late Miocene Hualapai Limestone deposit is overlain by a conformable alluvial gravel unit with signatures consistent with the Colorado Plateau material, whereas the Hualapai itself shows no evidence of streamflow consistent with the Colorado River (Blair and Armstrong 1979). This distinction indicates that the Hualapai Limestone was the last unit to be deposited prior to incision of the Colorado River, and thus the earliest timing of incision of the Colorado River must be less than 5.97±0.04 Ma to postdate the deposition of the Hualapai Limestone Member (Spencer et al., 1998). Therefore, our study can place a lower constraint on the timing of the incision of the tributary valley off Convulsion

canyon to 5.97±0.04 Ma. More information on the geological background of the Colorado River and surrounding region can be found in Appendix A.

3 METHODS

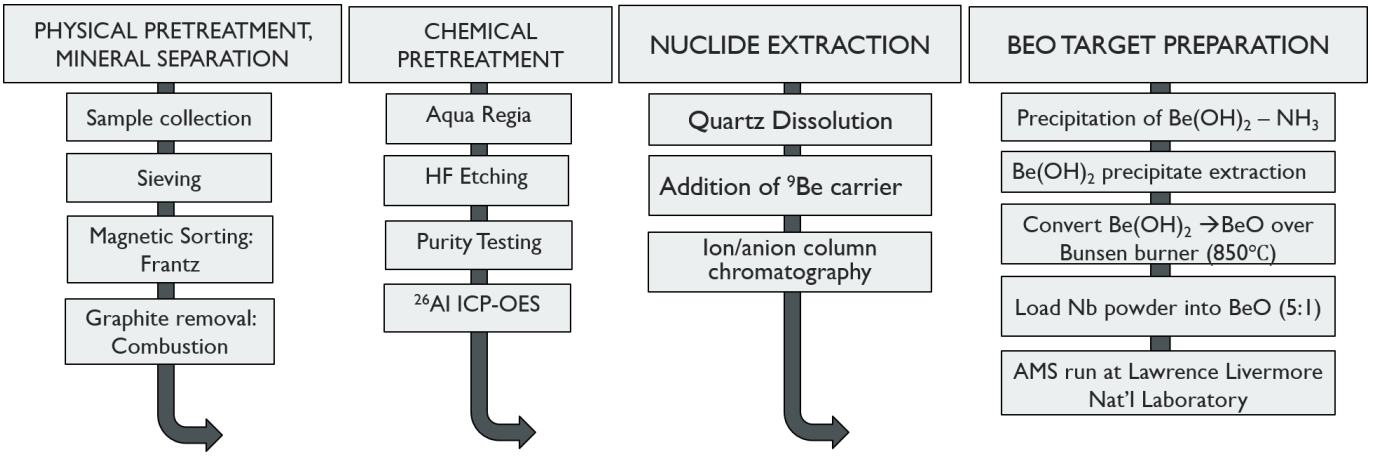

Figure 3-1. Flowchart for the methods used in this thesis. Four main types of processing were used; physical pre-treatment & Mineral separation, chemical pre-treatment, nuclide extraction, and BeO target Preparation.

3.1 GEOLOGICAL SETTING OF STUDY AREA

The Wasatch Plateau where the Convulsion Canyon is located in the northern Colorado Plateau's Uinta Basin Region. This geographic area has been understudied in regards to understanding the early incision of the Colorado River. The majority of work has taken place in the southwestern Grand Canyon section over the last century (Anderson et al. 2000, Pederson et al. 2002a, 2002b, 2013b, 2013c, Garvin et al. 2005, Karlstrom et al. 2008).

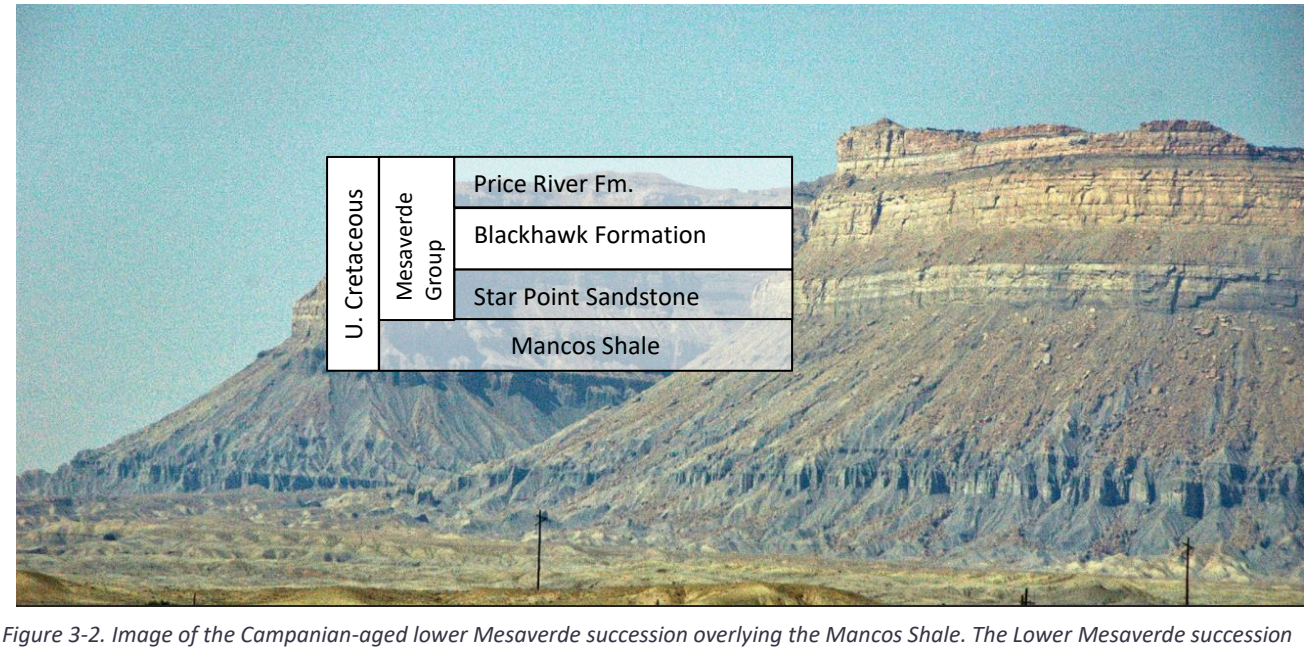

Figure 3-2. Image of the Campanian-aged lower Mesaverde succession overlying the Mancos Shale. The Lower Mesaverde succession houses the Starpoint Formation, and the Blackhawk Formation (image: Marli Miller, Getty Images).

The Upper Cretaceous Blackhawk Formation consists of interlaid sandstone and bituminous coal seams. The Blackhawk Formation was deposited during the Campanian in the Upper Cretaceous Period along the western coastal margin of the Western Interior Seaway. The Blackhawk Formation, as part of the greater Mesaverde Group, is part of a regressive sequence of repeating coastal intrusions, deltaic deposits, and coastal lowland swamps (Dubiel et al., 2000).

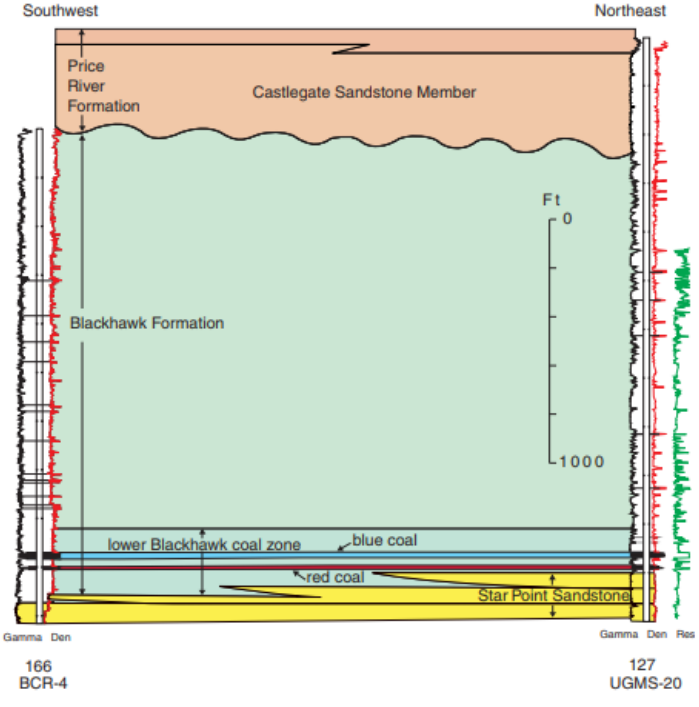

Figure 3-3. Stratigraphic correlation of two wells locating the depth and relationships of the red coal (Lower Hiawatha Coal Seam), blue coal (Upper Hiawatha Coal Seam) of the Upper Cretaceous Blackhawk Formation, unconformably overlain by the Castlegate Sandstone Member. The sample material in this thesis was collected from the lower Blackhawk Formation, directly over the blue coal (Dubiel et al., 2000).

3.1.1 Sample Collection

Two sets of samples were collected from two mines along the Book Cliffs; six SUFCO Mine samples were processed in this thesis, while the two Dugout Canyon Mine samples were not included due to large contamination of non-silicate material; they will not be discussed

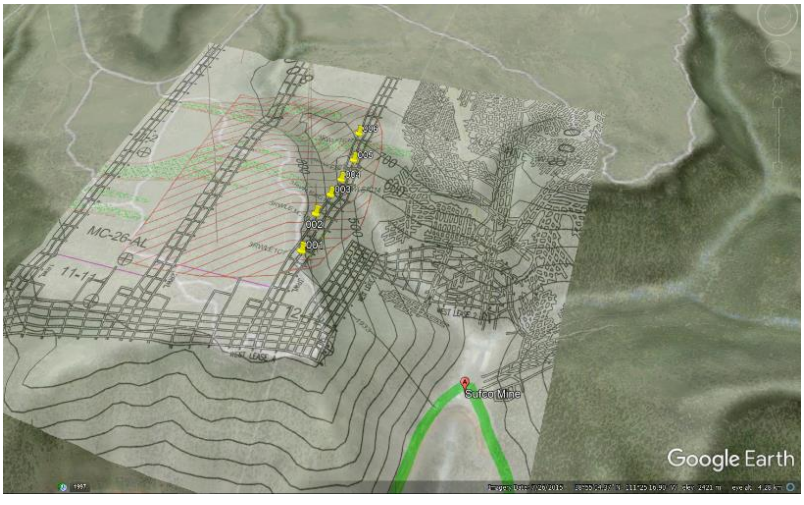

Figure 3-4. Overlay of sample transect from SW to NE end of valley incision overlain on topographic profile of the valley. The six sample sites are identified by the yellow pins (Google, 2017)

further in this thesis. Sample collection was done by A. J. Hidy (Lawrence Livermore National Laboratory) at the SUFCO Mine in Utah. The six samples were collected from a mine stope targeting the Upper Hiawatha Coal Seam made accessible through permissions given by the Canyon Fuel Company operating out of SUFCO Mine (Fig. 3-4). The sample material consists of sandstone sourced from crevasse splay deposits with an average porosity of 20 – 30%, and a bulk density of 2.20 g cm^{-3}. The mine stope runs laterally across the incision along a N-S trend at an elevation of 2343 m, a depth of 130 m below the bottom of the incised valley above (Fig. 3-5). The samples then underwent partial physical processing by A. J. Hidy. Sample SUFCO- 006 was not included in the late-stage chemical processing due to time constraints and a high-level of non-silicate contamination. Advanced physical processing, including mineral separation took place at the CRISDal Laboratory at Dalhousie University. The five remaining SUFCO samples consist of arenite sandstone material with the minor presence of Fe- garnet, hornblende, and potassium feldspar, as well as coal fragments. Generally, the quartz percentages ranged from 80% to 45% of the original samples.

3.2 Physical and Chemical Pre-treatment Procedures

The overlying objective in the physical and chemical treatment is to (1) remove all possible non-silicate contaminants from the samples; the production rate of ^{10}Be in quartz is very

well known and can be used later, then (2) to remove silicate material from the pure quartz to isolate ^{10}Be. This is done to reduce the sources of analytical error associated with the AMS run and the effect chemical impurities have on the current strength of the beam and the efficiency of the AMS run for the interpretation of the final ^{10}Be counts. A reduction in analytical error will contribute to obtaining the most accurate isotopic age.

3.2.1 Sieving, Magnetic Separation, and Combustion

The samples underwent sieving by A. J. Hidy for one grain size fraction (250-500 μm), and three grain size fractions at the CRISDal Lab (<150 μm, 150-250 μm , and >250-500 μm). The optimal grain size selected for chemical processing following physical processing is 250-500 μm; this grain size is large enough to withstand HF treatment, finer grain sizes will have a greater surface area per volume and are more susceptible to unintended dissolution. Before each sample is magnetically sorted on the Frantz up to 1.7 A, more impure, or 'dirty' samples are initially magnetically separated with an REE magnet.

3.2.2 Graphite Removal: Combustion

Following the magnetic separation, we tested a new method to remove coal fragments. This innovative carbon removal method is simple and efficient at eliminating carbon-based material from sample. To test this method, we selected sample SUFCO-006, a sample that had been prewashed and leached by A.J. Hidy that also had the highest percentage of carbon-based contaminants. The sample was dried in an oven overnight at 110℃, and combusted in ultraclean crucibles in a furnace for ~5-6 hours at 450℃ (Fig. 3-6). Samples were tested at 550℃ for 5 hours, but concern over quartz aggregate damage from the heat of combustion lead us to proceed with 450℃ for the remaining five samples. Sufficient warming and cooling times were allowed before and after combustion commenced, and were measured directly with an Infrared Temperature Gun™. The crucibles used to house 5-10.000 g of sample were washed with diluted soap, rinsed well with Type 2 water, then soaked in a 2% HNO_3 bath for one hour, then air dried

Figure 3-5. Furnace used to combust samples 001 - 006 at 450℃ for 5-6 hours to remove carbon material from sample (Soukup, 2017).

until use. With this technique, we saw a reduction in carbon content from 15% to ~1-3% when tested on the five crucibles obtained from sample 006. On iron-cemented samples, post-burn results showed a distinct red-tinge discoloration of the sample material. This oxidized iron is removed entirely during later chemical treatment.

3.3 CHEMICAL PRE-TREATMENT

As discussed in the previous section, to isolate ^{10}Be in the sample, two mineral removal stages take place; first, physical pre-treatment takes place to remove any non-silicate or magnetic grains or interstitial material. Then, Be is isolated in the pure quartz sample to be prepared for the targets. Sub-boiling distillation of HF, HCl, HNO_3, and H_3PO_4 takes place concurrently with the physically processing to collect as much ultrapure acid for the leaching process. Though high-grade acids are available, the degree of acidic purity required for our samples is very high, even higher considering we expect only hundreds of atoms of ^{10}Be per gram, and all precautions must be taken to ensure we do not introduce any foreign contaminants, including ^{10}Be or ^{9}Be into the sample during digestion.

3.3.1 Aqua Regia

Aqua Regia, which is an acid mixture with a ratio of 3HCl: 1 HNO_3, is applied to the physically treated samples to digest soluble minerals, soften and leach micas, and weaken grain boundaries. The quartz-dominated sample material is heated on a hotplate at 400℃. The resultant liquid, usually orange/brown in color is an iron-rich solution and is decanted, neutralized, and sent to waste using standard operating procedures for the CRISDal labs.

3.3.2 Hydrofluoric Acid (HF) leaching

Following an Aqua Regia treatment on the samples, HF leaching of the cleaned quartz takes place. This is done to further remove micaceous material and other unwanted silicates using a chemical mixture of 2 parts HF to 1-part H_2O. Heated to 75-80℃, the produced solution will turn a murky yellow green if solution is left-over from the previous Aqua Regia procedure. Following these two partial digestion steps, the resultant quartz material is tested for Aluminum purity using ICP-OES. The presence of high concentrations of Al (>100 ppm) indicates that the sample is not sufficiently clean for an AMS run, and could indicate the presence of silicate cementation of the quartz aggregates, and therefore dictates how we proceed with sample purification and target preparation. Once Al and Ti (and selected other cations) concentrations in the quartz are less than 100 ppm, so that the ion exchange sites on the resins are not completely

filled, we can assume that the sample is sufficiently pure to produce a pure AMS target and to use the production rates of 26Al and 10Be in quartz for the age or erosion calculations.

3.4 NUCLIDE EXTRACTION

The five remaining SUFCO samples are separated into six samples with the duplication of sample SUFCO-001 due to its large mass. The six samples, including the process blank undergo identical preparations methods from this point onwards. Following sufficiently low readings of Al concentrations, the pure-quartz samples undergo three stages of Nuclide Extraction, (1) Quartz digestion and ^{9}Be spiking, (2) anion column chromatography with controlled precipitation, and (3) cation column chromatography and controlled precipitation. Following the column chemistry, the sample target is prepared, masses are recorded, and the vials are prepared for shipment to Lawrence Livermore National Laboratory.

3.4.1 Quartz digestion & ^{9}Be Spiking

During the quartz dissolution phase, acid-cleaned Teflon™ beakers, rather than glass beakers are used, as glass contains the ^{10}B isobar that would be digested by the HF, and any uncalculated addition increases uncertainty in our final ^{10}Be concentrations derived from the ^{10}Be/^{9}Be ratio. Approximately 50.0000 g of pure quartz sample is added to each Teflon™ beaker, where the ^{9}Be carrier, with a known mass of 279 µg mL^{-1} of ^{9}Be, is added to each sample and the process blank giving an exact known number of ^{9}Be atoms, and a known (miniscule) number of ^{10}Be atoms. The ^{9}Be carrier is added to the sample to increase the oxide mass for the AMS run to determine the ratio of ^{9}Be/^{10}Be following AMS processing.

With the addition of the carrier to all samples, each sample undergo acid digestion by 20 ml of concentrated ultra-pure HF; 1 ml of $HClO_4$, and 5 ml of Aqua Regia per 5 g of quartz sample. Following their digestion at 125℃ for 1-4 days, the samples are dried for 1-2 days. During the actual digestion of the quartz, we have a lot of HF. So the HClO4 was added because it has a higher boiling point, so any remaining HF can be evaporated. Then HNO3 is added after drying down (three times) to get rid of the perchloric acid...By the end of the third dry-down, the Si is gone, and the cations form nitride salts. Three more rounds of acid digestion with $HClO_4$,

HNO_3, and HCl take place before the samples can be cooled, and transferred out to 15 ml vials and centrifuged at 1500 rpm for 15 minutes, vortexed, rinsed, and repeated again

3.4.2 **Anion & cation** Column Chromatography

Cation and anion column chromatography is done to remove the ion contaminants still in the sample after the acid leaching. The resin used for the columns removes unwanted elements and ionic complexes. The precipitation of the dissolved samples occurs after the columns have been conditioned by three rounds of increasing molarity of HCL for anion columns, and three rounds of decreasing molarity for the cation columns.

Figure 3-6. Anion column chromatography taking place to remove contaminant anions from the sample (Soukup, 2018)

3.5 TARGET PREPARATION

Following pipetting of centrifuged samples, controlled precipitation isolates the $Be(OH)_2$ solution, which is removed from the vials and put into high purity low-Boron quartz vials. These glass vials containing the solution are then burned over a Bunsen burner for several minutes in order to convert the $Be(OH)_2$ in liquid phase into BeO in solid phase. This mass is measured in the glass vials post-burn, and then placed into a stainless-steel target. Nb powder is added to the solid BeO mass at a 3:1 volume ratio and mixed sufficiently to ensure even mixing. A well-mixed powder has a higher guarantee of creating an even current during the AMS run.

The steel targets require very specific packing (Fig. 3-9); above the Nb-BeO mixture, a volumetric cube of space must be present between the top of the mixture and the base of the target cone. This cubic space is designed to create maximum efficiency for the trajectory of incoming Cs atoms displacing the Nb and BeO atoms and projecting them towards the AMS**.** Six samples and one process blank are taken to Lawrence Livermore National Laboratory (LLNL) following BeO target preparation and run 3-4 times through the AMS. This long run time is done to reduce the amount of error in age constraints by allowing as many ^{10}Be atoms to ionize as possible.

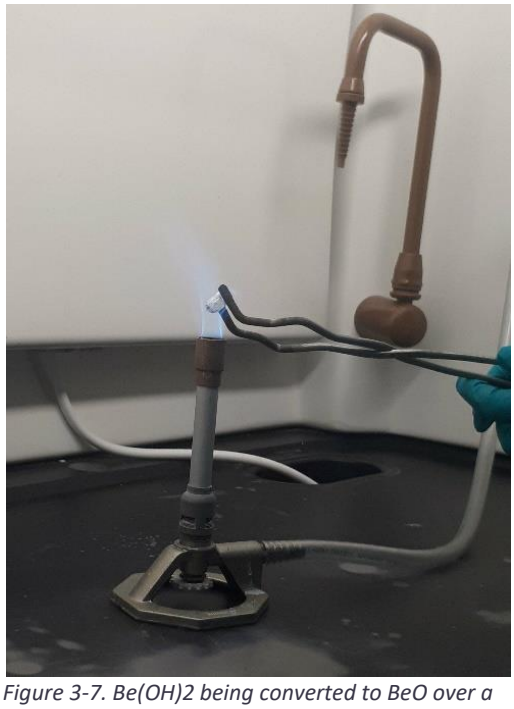

Figure 3-7. Be(OH)2 being converted to BeO over a Bunsen™ burner at 750- 850C flame (Photo: M. Soukup, 2018)

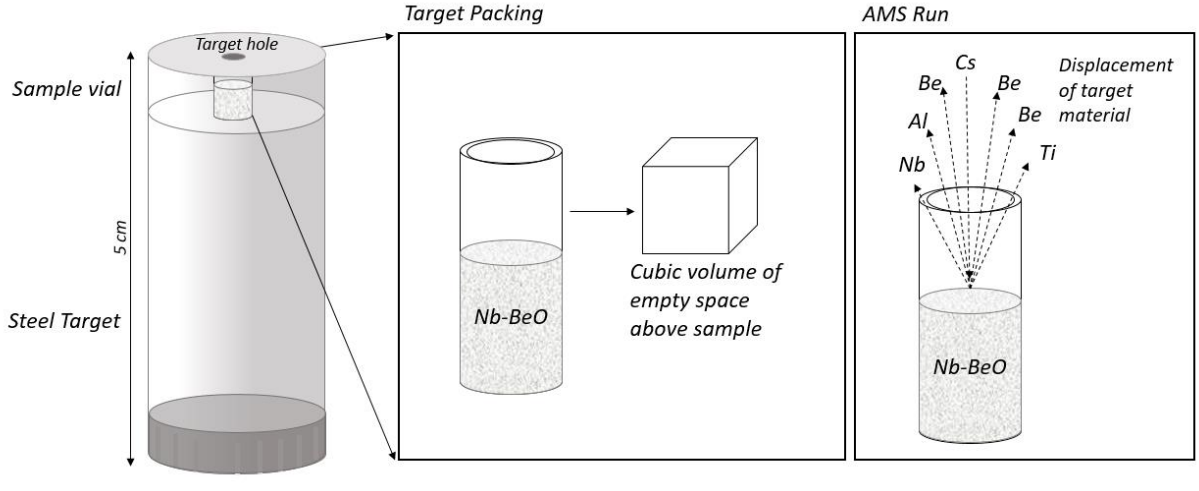

Figure 3-8. Diagram of AMS target preparation and packing, and the process where Cs ions are accelerated towards the Nb-BeO mixture to displace the mixture and begin the acceleration process.

3.5.1 **Accelerator Mass Spectrometry (AMS)**

AMS works by isolating ^{10}Be atoms with chemical and magnetic parameters in order to produce an age from the ^{10}Be isotopes in sample. Basic principles of AMS include ion extraction by Cesium sputtering in the source (Fig. 3-8), the rejection of non-desirable isotopes, particle acceleration, rejection of isobaric ions, and rare isotope counting. The low efficiency of the AMS, which is around 1-2%, is a function of isotope spectroscopy equation,

$$R = \frac{mv}{QB} \quad (1)$$

where mass, m, velocity, v, charge, Q, force magnetic, B to solve for the radius, R of the magnet necessary to achieve the highest efficiency in the particle beam's path towards target. Isobar separators can clear up the mess of impurities in the sample using resonance frequency to minimize isobars (such as ^{10}B for ^{10}Be), but with an further undesirable reduction in efficiency.

The analysis of the six samples took place over an approximately 3-hour period. Before the official recorded sample run for each target, a sputter source directs Cs at the BeO-Nb target to complete a warm up 'burn in.' This occurs on the surface of each sample for 30 s. After this, the material is electrically directed into the AMS Van de Graff Tandem Accelerator with terminal voltage set at 8.3 MV and accelerated by a high voltage terminal, and then through a post-stripper to dissociate molecules. Following this stage, the particle paths are controlled by magnetism that arcs particles with the desired mass and charge towards further sorting stages (fig. 3-10). One of these sorting technologies is removal of contaminants by post-strippers. These work by blocking the path of specific subatomic material that does not fit desired charge and mass criteria. For example, the carbon-foil stripper that has been recently added (Fall 2017) to the AMS line at LLNL effectively removing 98% of incoming ^{10}B atoms that would otherwise decrease the precision of counted ^{10}Be atoms due to their very similar identical mass. The carbon foil stripper consists of a thin sheet of atoms spaced at intervals equivalent to a 4+ charge. This spacing allows the majority of the smaller 4+ ^{10}Be atoms to pass through, while the larger 5+ ^{10}B atoms are stopped by the foil. This removal of isochronal material, though effective in its effect on ^{10}B, does decrease the efficiency of the AMS line because of the likelihood of the 4+ ^{10}Be atom being stopped 20% more of the time (4+/5+ leads to 80% transmission) compared to if no carbon foil was in place. The sorted ^{10}Be particle then travels through the remainder of the accelerator and ionizes in the gas chamber where it is detected at a rate of 2 counts per second (cnts/s) or less.

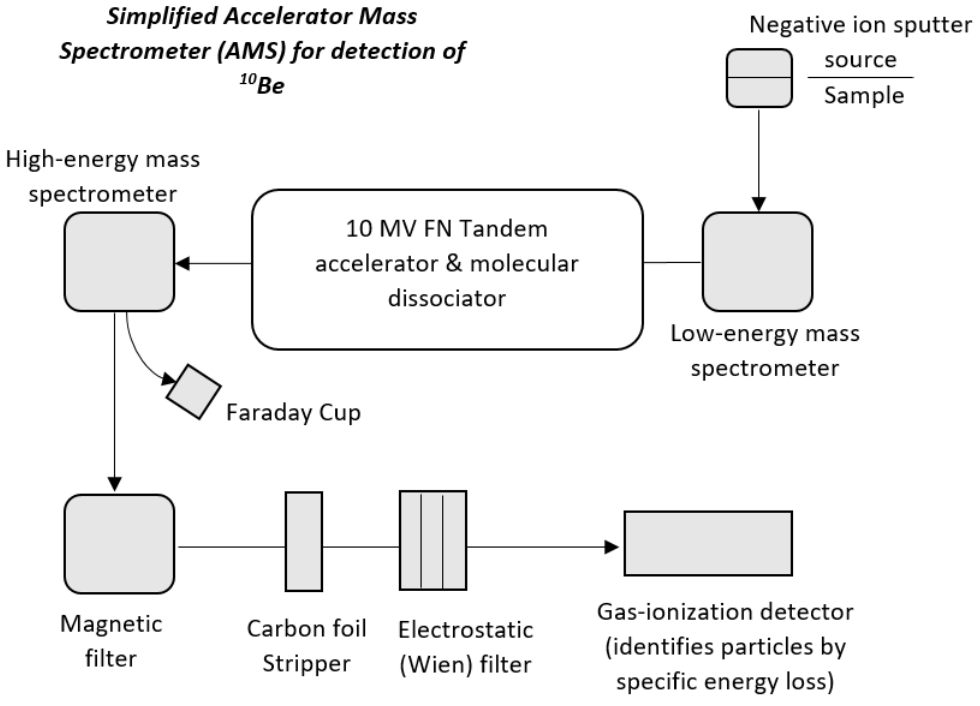

Figure 3-9. Simplified diagram of a conventional Accelerator Mass Spectrometer (AMS) used to detect ^{10}Be. The samples are placed at point A, and are ejected from the target by collision with incoming Cs particles from a source. They then move through a low-energy mass spectrometer, are sorted by magnetic lenses and accelerated in the Tandem accelerator. They proceed through the high energy mass spectrometer that removes and collects particles that do not have sufficient mass to proceed on the desired trajectory. The beam of particles then passes through a magnetic filter that removes particles of insufficient charge. At this point in the trajectory, the remaining material in the beam is exactly the mass of ^{10}Be or have very similar characteristics, such as the isochron ^{10}B. the carbon foil stripper and Wein filter remove the majority of the surviving contaminant material and the purest-possible ^{10}Be beam enters the gas ionization detector where it is collected for data interpretation (Modified from LLNL by Soukup, 2018).

The collected size of samples of the mass fraction necessary for chemical and physical processing was sufficient for the preparation and collection of data. The mass necessary to adequately prepare the targets were decided upon 50.000 g each (Hidy, Pederson, Gosse 2018, private communication). This volume was available for samples 001 through 005. The reason that 004 and 005 produced data that was outside of our standard error is due to the presence of Fe-rich cement that could not be removed in time for the run. This negatively effected the current strength during AMS, and compromised the ^{10}Be count as they were collected from the run. Future work will include more cleaning and purification of these samples so they can be run later and be incorporated into the data and interpretation.

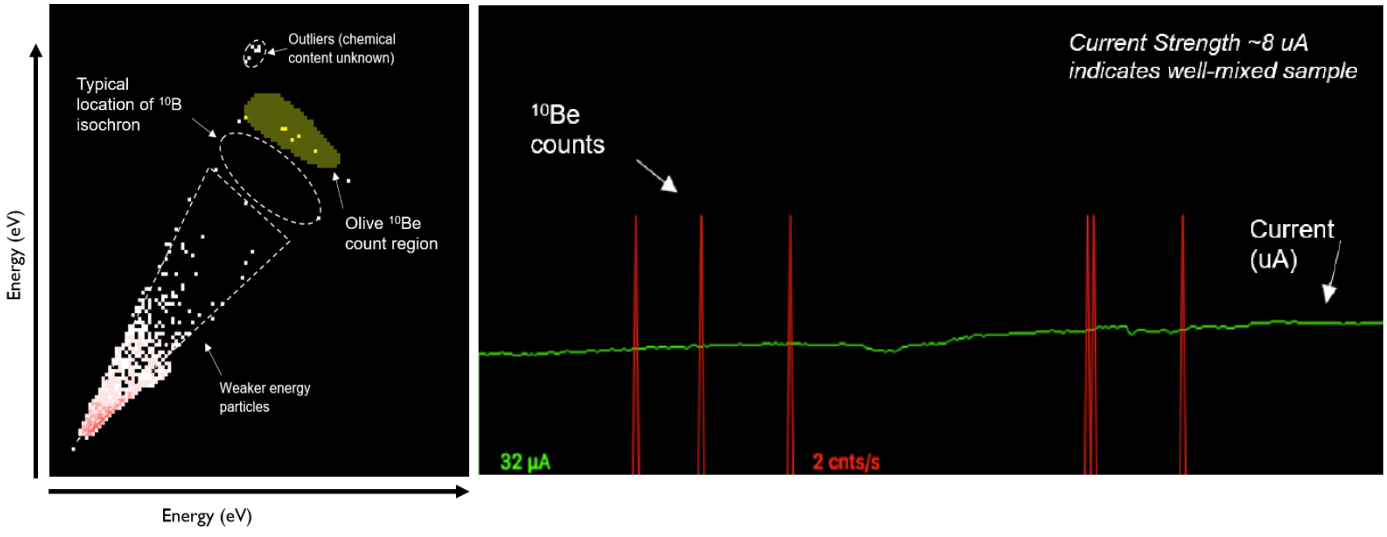

Figure 3-11. (left) energy distribution of ionizing particles from the AMS beam. The olive oval indicates ^{10}Be counts obtained from the run. (right) Current diagram for sample 001 ran at LLNL in January 2018. The samples current is approximately 8 uA, and is stable, indicating an evenly mixed Nb-BeO sample.

3.5.2 **Accelerator Mass Spectrometry (AMS) Data Reduction**

Processing of six targets and one process blank at Lawrence Livermore National Laboratory yielded four values (one duplicated sample) and one standard value to be used to test the quality of our sample run. Our standard yielded very favorable ratios and currents, indicating that our ^{10}Be/^{9}Be ratio value and thus ^{10}Be concentration value will be highly sensitive, reducing our uncertainty and error for the determination of an erosion rate.

The first set of data received during the AMS run at LLNL show the benefit of high precision geochemistry during preparation, as well as meticulous attention to detail of sample vials, distribution, and analytical measurement. The Current strength (uA), identified by the near-constant green line in Fig. 4-1 for this run of sample 001 indicates that the Nb-BeO sample in the stainless-steel target was well-mixed. The strength of the Current for sample 001 is ~8 uA (on a scale of 32 uA). Normally we achieve ~ 25 uA. So, a reduced current is likely caused by a combination of a lower transmission due to the post-Tandem stripper, and possibly due to more contaminants in the BeO target than usual.

The energy cone in Fig. 4-1 presents the increasing strength of the incoming ionizing particles towards the top right corner. The olive bubble shows the energy parameters characterized for ^{10}Be counts based on incoming energy. The collection of points towards the

lower left corner are a large occurrence of weaker particles that do not fit the parameters of ^{10}Be counts. Normally in AMS runs for ^{10}Be, a band of ^{10}B counts (which is an isochron of ^{10}Be that can effect the accuracy of ^{10}Be counts) is present slightly below the olive bubble. The distinction between ^{10}Be and ^{10}B is important to decrease uncertainty in counts. with the implementation of the carbon foil stripper mentioned in 3.5.1, the Boron correction value is not significant for our calculations. For more information on the current strengths and ^{10}Be/^{9}Be ratios obtained in AMS, please see Appendix D.

3.5.3 Calculation of ^{10}Be Concentrations, Production Rates, and Erosion Rates

This section consists of the raw data calculation that goes into obtaining the three main quantifiable results of this study; (1) concentration of ^{10}Be in atoms g^{-1}, (2) production rates of fast muons at depth in atoms g^{-1} yr^{-1}, and (3) erosion rates in mm Ma^{-1} and km Ma$^{-1)}$ Each of these results are evaluated with sets of parameters that are taken from a variety of peer-reviewed sources. For more information on numerical values of each calculated parameter, please see Appendix E.

3.5.4 **Calculation of final ^{10}Be Concentrations**

To produce the final ^{10}Be concentrations for the six samples processed at LLNL, three stages of calculations took place. To begin, the ^{9}Be carrier data needs to be incorporated with the pure quartz data. The variables needed are the carrier ^{9}Be mass (g), carrier concentration (mg ml^{-1}), carrier density (g ml^{-1}), and the added ^{9}Be number of atoms. A high purity Be carrier was prepared at CRISDal from a phenacite crystal extracted from a deep mine under the Ural Mountains, and it contains very little ^{10}Be (typically zero or one counts of ^{10}Be over 400 seconds of AMS analysis with 26 uA currents). Enough carrier is added to deliver approximately ~10^{19} atoms of 9Be.

Error correction is a very crucial area of measurement. Normally during an AMS run, there is a need for a Boron correction variable to be applied to the Total Analytical Error (TAE). This is because of the similar mass and charge of ^{10}B, which an isochron to the ^{10}Be. During the end-stage ionization of remaining atoms in the AMS beam, ^{10}B is not fully differentiable from ^{10}Be, and can complicate counting of ^{10}Be for marginal energy values of both ^{10}Be and ^{10}B. As discussed in 3.5.1, LLNL recently implemented a carbon-foil stripper that acts as a fence to sort and stop ^{10}B from passing, while letting ^{10}Be pass through. This is achieved by taking advantage of the differences in atomic numbers of ^{10}Be and ^{10}B. Where ^{10}Be has an atomic number of 4, ^{10}B has an atomic number of 5. Thus, the slightly larger mass of ^{10}B prevents the majority of

incoming ^{10}B to pass through the '3-D forest' of the carbon foil stripper. The reduction in the amount of ^{10}B in the ionizer has both positive and negative effects on the final ^{10}Be counts. With more obstacles obstructing ^{10}Be atoms accelerated through the AMS in combination with the already very low system efficiency (~1.07% Hidy et al., 2017), the efficiency of the beam is further reduced. The carbon stripper does positively affect the differentiation of ^{10}Be counts from undesirable counts by eliminating 80% (4 protons/5 protons) of incoming ^{10}B.

Other error corrections for the produced ^{10}Be/^{9}Be ratios include the ^{10}Be/^{9}Be blank error, the number of ^{10}Be atoms in the Blank, and the 1σ error value derived for the ^{10}Be/^{9}Be Boron correction, the number of ^{10}Be atoms present, and the ^{10}Be blank correction. Total Analytical Error is presented in the following equation:

$$Total\ Analytical\ Error\ (TAE) = 10Be\ atoms\ Blank\ Correction \left((1\ \sigma\ error)^2 + \left(\frac{10Be\ in\ Blank}{10Be\ atoms} * \frac{\frac{10Be}{9Be} Blank\ error}{\frac{10Be}{9Be} Blank\ Boron\ Correction} \right)^2 \right)^{\frac{1}{2}} \quad (2)$$

Then to calculate the 1 σ TAE, the following equation is employed:

$$1\ \sigma\ TAE = \frac{TAE\ 10\text{Be}\ atoms}{10Be\ atoms\ Blank\ Correction} * 100 \quad (3)$$

Following the calculation of TAE, the final ^{10}Be concentration values for each sample are calculated. The measured concentration error of this value is equivalent to the 1σ TAE described above, and can be applied in both cases. The final ^{10}Be concentration value that will be used in later calculations to find the fast muon production rate and the erosion rate is determined from the measured concentration (^{10}Be atoms g^{-1}) subtracted from the concentration of contaminant material that was not removed in AMS, such as ^{10}B. Due to the near-total removal of ^{10}B from the carbon foil stripper implementation, the contaminant concentration for these samples is assigned a value of 0 atoms g^{-1}, therefore:

$$Measured\ concentration\ (10Be\ atoms\ g^{-1}) = \frac{10Be\ atoms\ Blank\ Correction}{Quartz\ Mass} \quad (4)$$

It is important to convey here that we measure $^{10}Be/^{9}Be$ for each sample. We also measure a standard with known $^{10}Be/^{9}Be$. The measured value is never exactly the same as the accepted value. The fractional difference between the accepted/measured standard ratios is the normalization factor. We then multiply that normalization factor to get adjust the measured sample ratios for any small effects that happened during the run or tuning. Using that normalized $^{10}Be/^{9}Be$ for a sample (10^{-15}), we multiply by the number of ^{9}Be atoms (10^{19}) to get 10^{4} atoms of ^{10}Be.The 1σ error calculation then takes into consideration any possible remnant contaminant concentration as presented in the following equation:

$$1\,\sigma\, Error\ Concentation\ (atoms\ g^{-1}) = (measured\ concentration\ error^{2} + other\ concentration\ error^{2})^{1/2} \quad (5)$$

Finally, the last stage of calculating the final measured ^{10}Be concentration of the sample is determining the fraction of the measured ratio that is blank subtracted with the following equation:

$$Blank\ Subtracted\ Fraction = 1 - \frac{10Be\ atoms\ Blank\ correction}{10Be\ atoms} \quad (6)$$

3.5.5 **Calculation of Muonic Production Rate Data**

The final ^{10}Be concentration data is applied to production rate calculations that have undergone scaling corrections based on the LSD Scaling model (Lifton, N., Sato, T. and Dunai, T.J., 2014). Two MATLAB scripts are used to quantify the variables based on several factors, which are Latitude, Longitude, Altitude, Atmospheric Model employed, Age of sample, Gravimetric Fractional Water Content, and Nuclide type. The role of this first script (*LSD.m*) is to generate the appropriate parameter values to apply as input values to the *LSDscaling.m* script. These two parameters are Cut-off Rigidity (GV) and Solar Modulation (MV).

The second MATLAB script is used to calculate the muon production at depth. It can be applied to a variety of nuclides including ^{10}Be, ^{26}Al, and ^{14}C, but for the purpose of this study it is used to calculate the muonic ^{10}Be production at depth. Eight parameters are used to calculate the muonic production at depth. They are *z*, the depth below the surface in g cm^{-2}; *h*, site atmospheric pressure (hPa); *Rc*, the cut-off rigidity (GV) and *SPhi*, the solar modulation parameter derived from the *LSDscaling.m* script; *nuclide*, which is the nuclide specified (^{10}Be) displayed as a numerical value (10); *consts*, which are structure-containing nuclide specific constants that specify either:

(a) *Consts.Natoms*: the atom number density of the target atom (atoms g^{-1})

(b) *Consts.k_neg*: the summary cross-section for negative muon capture (atoms $muon^{-1}$)

(c) *Consts.sigma190*: the 190 GeV cross-section for fast muon production (cm^{-2})

3.5.6 **Calculation of Erosion Rates**

Using the final ^{10}Be concentration values, and the fast muon production rate calculated in the previous section, two equations are employed for determining the erosion rate in this study. In order to calculate erosion rate Ɛ, first the production rate of the sample at depth must be calculated,

$$P_{\mu f}^{n} = P_{\mu f}^{0} * e^{-\frac{z\rho}{\Lambda}} \quad (7)$$

where $P_{\mu f}^{0}$ is production rate of fast mouns at depth of the sample collected, $P_{\mu f}^{n}$ is the calculated fast muon production rate, z is the depth of sample measured in g cm^{-2}, ρ is the bulk density of the material above the sample in g cm^{-3}, and Λ is a constant, the approximate attenuation length of fast muons, which is 4320 g cm^{-2} (Heisinger et al. 2002b). The reason the attenuation length is approximate is because further work needs to be done to calibrate its value, obtained experimentally, with field data. The resulting fast muon production rate determined at depth of the sample is then incorporated into the erosion rate equation,

$$\varepsilon = \left(\frac{P}{N} - \lambda\right)\frac{\Lambda}{\rho} \quad (8)$$

where ε is the erosion rate in cm yr^{-1}, P is the fast muon production rate at depth in atoms g^{-1} yr^{-1}, N is the concentration of ^{10}Be in atoms g^{-1} calculated previously. This equation will present the erosion rate in cm yr^{-1}, and this is converted into mm Ma^{-1} by multiplying the erosion rate equation by 100,000.

4 Results

To characterize the functional application of measuring ^{10}Be produced from muonic interactions at depth, we selected a study site that was accessible at a great depth, and where samples with quartz-rich material could be obtained. On the basis of these results we hypothesize that ^{10}Be concentrations could be obtained from depths greater than 130 m below modern topography with replicable results and within an uncertainty of 20%.

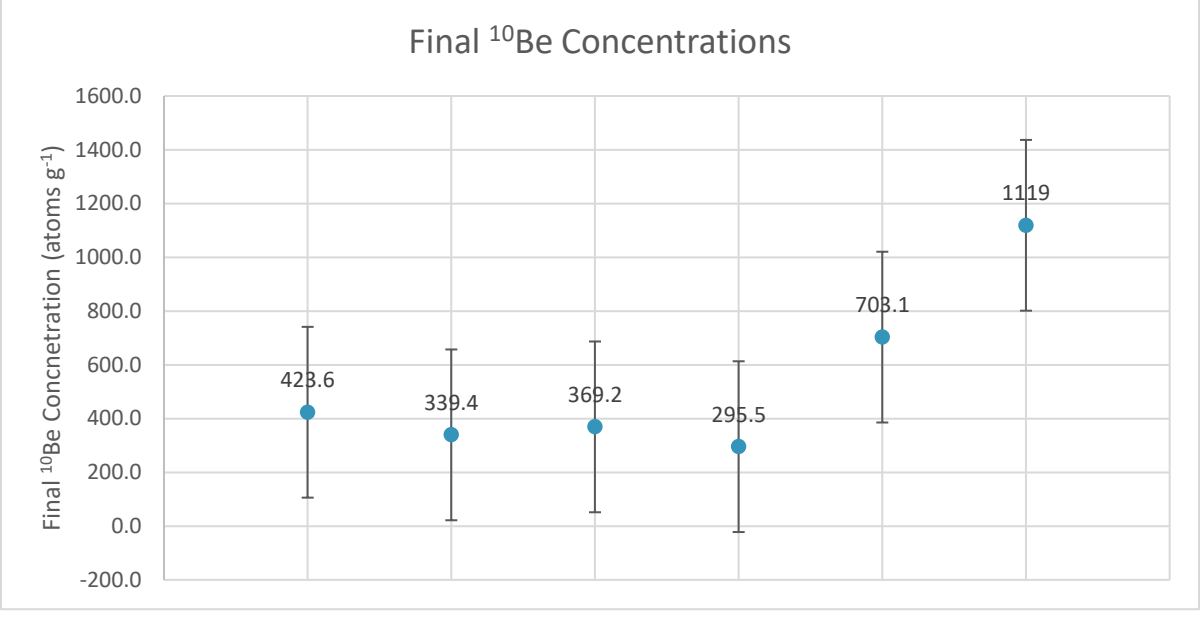

Figure 4-1. Graph showing Final ^{10}Be concentrations in atoms g^{-1} against samples 001 – 005 (left to right). The error bars represent 1 sigma uncertainty based on calculated ^{10}Be concentrations. Note the accuracy of samples 001 and 001-DUP, demonstrating the reproducibility of this method across other samples that underwent the same chemical processing (Soukup, 2018).

This sample material underwent physical and chemical pre-treatment yielding ultrapure quartz from an arenite sandstone with 15% coal and 3% other mineralogical impurities. The calculated ^{10}Be concentration values range between 423.6 ± 0.1850 g^{-1} and 1119 ± 0.3013 atoms g^{-1}, with a standard deviation of 317.6 atoms g^{-1}. Calculated concentrations of ^{10}Be from AMS/Data reduction were used to extrapolate the production rate of ^{10}Be from fast muons at depth, which ranged between 7.54e-4 atoms g^{-1} yr^{-1} to 1.80-4 atoms g^{-1} yr^{-1} with a standard deviation of 4.26e-4 atoms g^{-1} yr^{-1} (Fig. 5-1). Due to the assumptions that were necessary to resolve the erosion rate, the found erosion rate values are multiple orders of magnitude too large for our incision. Despite this, the erosion rate trend across the transect inversely mimics the

overburden thickness above the samples. This indicates that this method has produced evidence that can roughly interpret relative amounts of erosion over time.

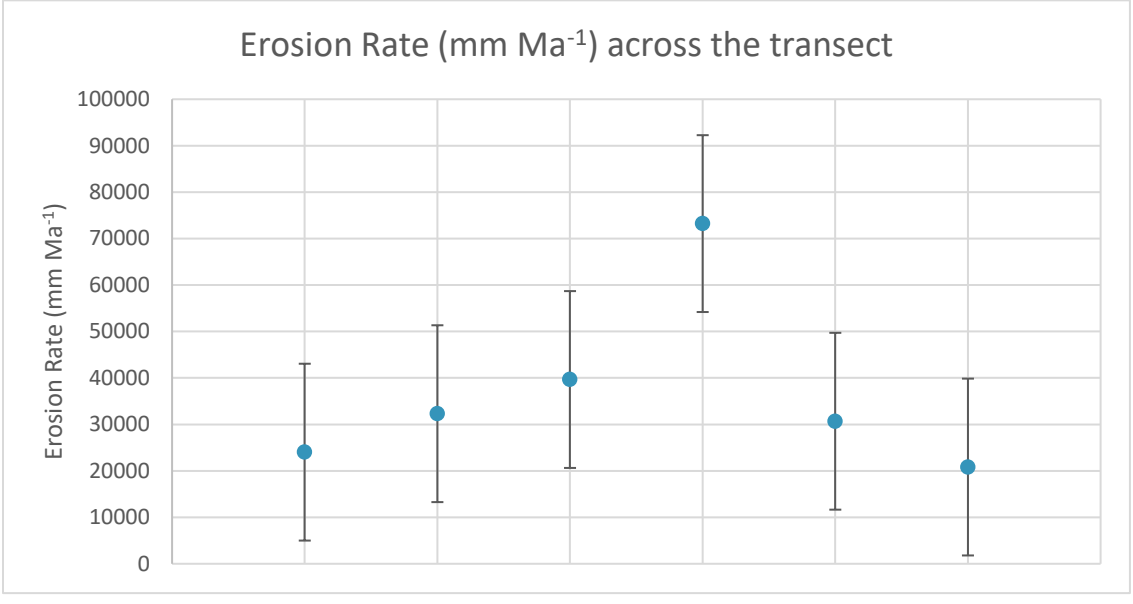

Figure 4-3. Graph showing the variation in erosion rates (cm yr-1) observed at a depth of at least 130 m below the SUFCO Mine incision; the transect trends S-N with samples 001 – 005 (left to right). This graph inversely mimics the shape of the topography over the incision, with the highest rate of erosion located where the topography is the shallowest.

The replicability of the obtained ^{10}Be concentrations is quantifiable based on the duplicate measurement of sample SUFCO-001. Uncertainties associated with sample duplication are within reasonable error of 18.5 – 20.9%, and the final ^{10}Be concentration values reflect the same results, where values of 423.6 ± 0.2 atoms g^{-1} and 339.4 ± 0.21 atoms g^{-1} .

5 DISCUSSION

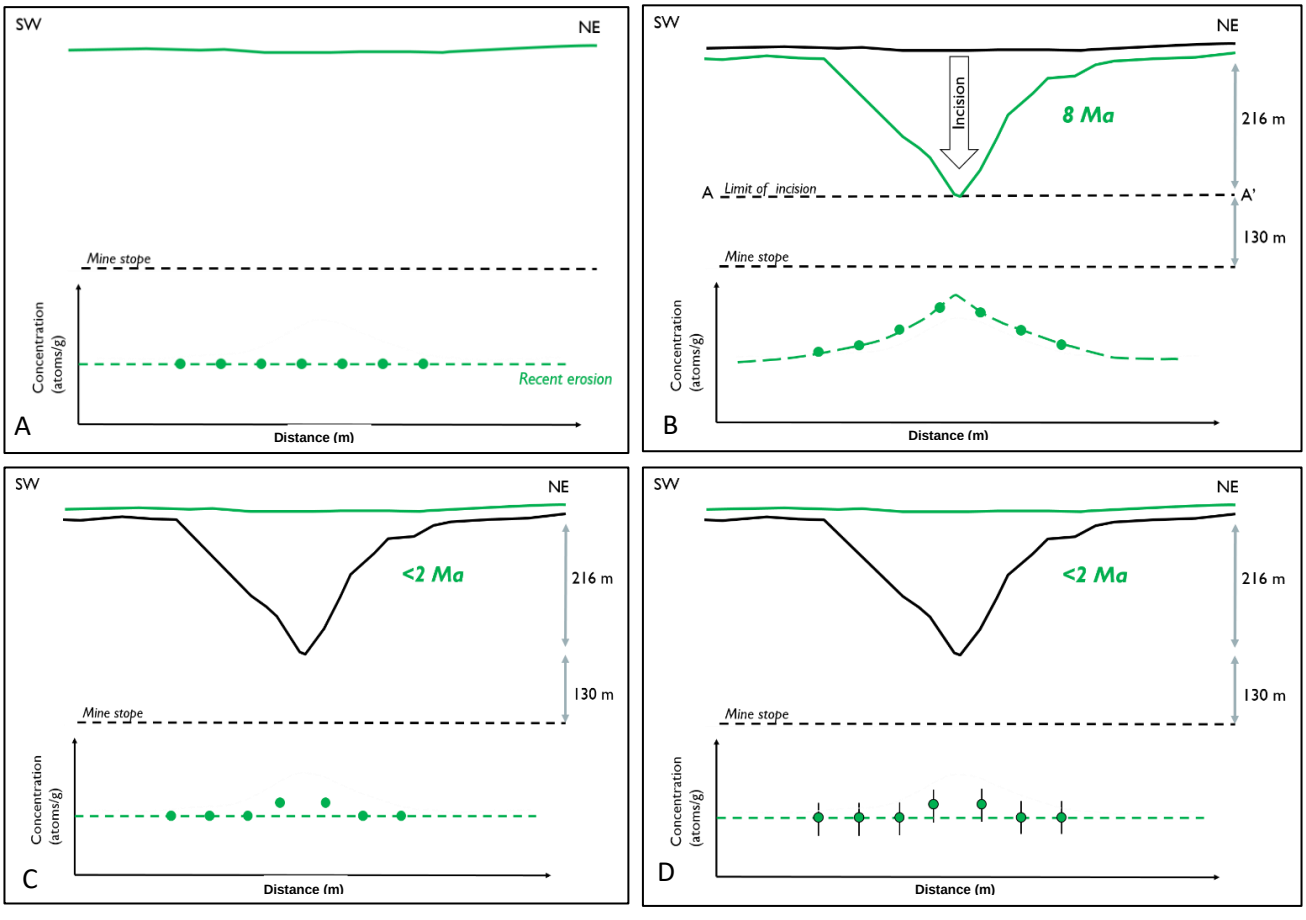

Figure 6-1. A shows a plateau surface that has not been incised. Therefore, the pattern of ^{10}Be concentration reflects a uniform and steady state erosion (constant, gradual) of the plateau, with no relief generation. Figure 6.1B is an end member scenario in which the incised valley already existed by 8 Ma and no further incision occurred since. The concentrations are not uniform, but reflect the shielding above each sample. Figure 6.1C represents a scenario in which the incision has occurred within the last 8 Ma. In this case the concentrations reflect a shielding effect that changes over time. the solid green line indicates the topographic profile above for the cases between all end-members, while the dashed green lines indicate the trend in ^{10}Be concentrations for each scenario. The solid black lines indicate mine stope depth, and limit of incision depth as denoted.

Recall our three potential scenarios of for hypotheses, each indicating the expected ^{10}Be concentration trend. These three scenarios indicate the expected trend in ^{10}Be concentrations at depth that would be consistent with recent erosion, late erosion, and median erosion. Additionally, in the fourth image, the case of median erosion age is expanded on with consideration for the degree of error in our samples.

Our results indicate a pattern of ^{10}Be concentration below the incision consistent with an erosion event occurring at a time later than 1 Ma, but earlier than 8 Ma, our end-stage member. The obtained ^{10}Be concentrations range from 295.5 ± 0.3 g^{-1} and 1119 ± 0.3 atoms g^{-1}, with a standard deviation of 317.6 atoms g^{-1}. This broad range in samples originate from the large error that inherently decrease the precision of the measurement of the ^{10}Be concentrations. These three

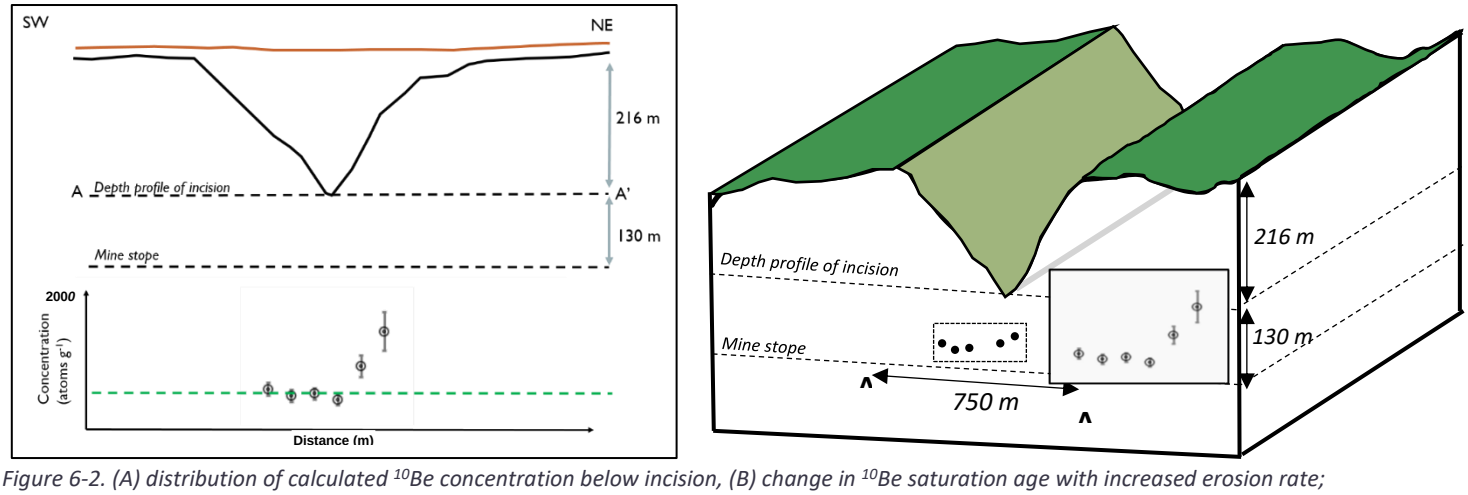

Figure 6-2. (A) distribution of calculated ^{10}Be concentration below incision, (B) change in ^{10}Be saturation age with increased erosion rate; if our data indicates faster erosion rates, ^{10}Be will reach saturation earlier, thus ability to precisely interpret erosion age will be limited earlier.

main sources of error are the AMS counting statistics error, the ^{9}Be Carrier error, and the Blank subtraction error. AMS counting statistics are derived from the errors that originate from the electromagnetic sorting process of the AMS. As the purpose of this AMS run is to isolate ^{10}Be, contaminants that were not removed in the chemical treatment are removed and collected during AMS. ^{9}Be carrier error is associated with the addition of the ^{10}Be atoms within the ^{9}Be carrier. If there are any (even miniscule) amounts of ^{10}Be atoms in the ^{9}Be carrier, then all samples will be affected by the addition of foreign ^{10}Be atoms. This addition, however small will influence the final ^{10}Be/^{9}Be ratio. Blank subtraction error is derived from the calculation of the assumed number of ^{10}Be atoms in the process blank, which should only have 0 – 1 ^{10}Be atoms (if any). Normally, during AMS, an average of 500,000 atoms are counted by the AMS. With our data, we counted on the order of 300 atoms. Therefore, the addition

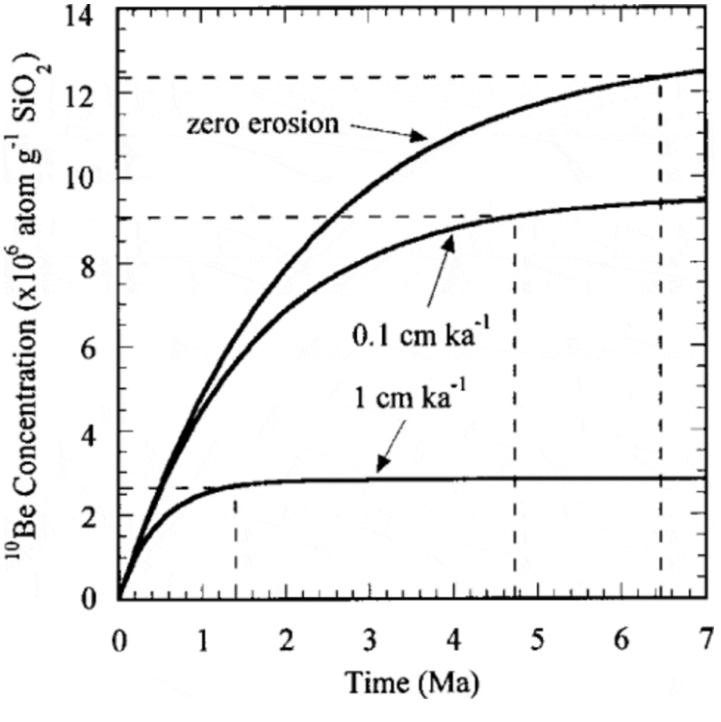

Figure 6-3. Plot of the effect of increasing 10Be concentration with respect to time. With increased erosion rate, the measurable 10Be decreases in a steady-state erosional system (from Fabel and Harbor, 1999)

of even one ^{10}Be atom will have a larger influence on the final error than for measurement of conventional ^{10}Be samples.

Based on the resultant ^{10}Be concentration trend from our data, which estimates that the incision event most likely occurred closer to 2 Myr, we can interpret that this northern incision occurred later than the earliest known incision of the Colorado River. The earliest recorded incision of the Colorado River is dated to 5.97 Ma from the Hualapai Limestone. Therefore, with the comparative ages of 2 Ma and ~6 Ma, the results the incision in the north, farther away from the incision point of the Colorado River, is logically going to be younger than the initial establishment of the river downstream.

Additionally, this evidence of later erosion of the Colorado River upstream of the mouth of the Colorado River, is conclusive with the head-ward erosional theory of the development of the Colorado River Watershed. Following the establishment of the Colorado River incision downstream as dated from the Hualapai Limestone, head-ward erosion would have needed to occur moving north the Colorado River Watershed to achieve this significant difference in incision ages.

The predominant objective for studies in the past of muonic production at depth have been to confirm the experimental production rate values with field values, as not enough data currently exists (Granger and Smith 2000, Heisinger et al. 2002a, 2002b, Borchers et al. 2016). In addition, all previously conducted studies were largely confined to depths of < 50 m, with the exception of Kim et al., 2004, which reached a depth of ~197 m. the shallow depths of previous comparative work contributes to the knowledge that fast muons can be measured to depths of 50 m, but does not speak to the viability of measuring fast muonic production at depths greater than 200 m with much peer-reviewed accuracy.

Of the existing literature, Kim et al., 2004 provides the best comparative techniques and results. Measurement of muonic production of ^{10}Be from surface to a depth of 49,300 g cm^{-2} (197.2 m) was conducted in a quartz vein in New Zealand. Though this study yielded uncertainties < 7% for ^{10}Be, uncertainties were only measured off of AMS counting statistics. Additionally, Heisenger 2002a,b presents fast and slow negative muon data from experimental production, but this presents an issue for our calculations, as his predictions work with muon energies (100 GeV, 190 GeV) much higher than produced naturally, and thus the CRONUS

calculator overestimates the production at depth where denudation is greater than 5 km Myr^{-1} (Balco et al., 2008).

5.1 LIMITATIONS OF THE STUDY

The limitations encountered in this research were not unexpected, fortunately. By approaching this study with an realistic objectives and highly precision analytical methods, we could interpret real data from a dataset that has not been previously proven to work at this low uncertainty at this depth; the presence of measurable data on their own is a success. The low-precision of the data was expected with the knowns of the inefficiencies of AMS, and the very small number of atoms of in situ-produced ^{10}Be that had not decayed out that were expected based on the depth at which the samples were collected.

The trending nature of this considerably small dataset allows for more generalization than would be present in studying material ay shallower depths with reduced uncertainties. As well, due to the lack of studies in the surrounding in the Uinta Basin region, the erosion rate obtained in this study can be applied as the very general erosion rate assigned to the region that can be incorporated into the models focused on understanding the variation and distribution of erosion rates across the Colorado Plateau.

Relative to the scope of the Colorado River watershed, our sample site was non-representative. Our site is located on the northern-eastern quadrant of the Colorado Plateau and lies in a region that has been poorly studied, but still in a region of low-end erosion rates. The likelihood that this incision would be linked with the largescale regional erosion of the Colorado River system seems logical, considering the large scope of the Colorado River watershed. The degree to which this incision was affected by the erosion of the Colorado Plateau is debatable, i.e. secondary, tertiary, etc. and the timing and order of this incision will be improved upon with further studies done in the areas, in addition to future work that will be built off of this study.

An additional limitation to our study area is the lack of regional exploration for records of regional incision association, and the fact that our depth profile is constructed from only three samples, or four data points. This dataset provides a view of change in concentration against depth, lateral distance etc., but only for the Northeast-facing valley. Due to time constraints and high-contamination of samples along the southwesterly facing slope, the samples were not sufficiently clean for the January 2018 AMS run. The lack of a full picture across the valley adds

uncertainty to the trend, but three points do present some workable data. On the contrary, our model is the only model that exists for this incision, and is thus the most complete version for this incised valley, and present data for 50% of the mine stope sample section. This provides us with the clearest picture of incision in the Uinta Basin region of the Colorado Plateau, and is a stepping stone for further work in the region.

6 Conclusions & Recommendations

The main concept we want to iterate with this study is that muon-induced TCN production can be measured at depth with adequate previous consideration of necessary sample purity and volume to estimate erosion rate, and to quantify ^{10}Be concentrations and production rates at depth. In addition, a sufficiently powerful Accelerator Mass Spectrometer (AMS) is necessary to collect the very low counts of ^{10}Be that is obtained from the run.

Geomorphologically, the interpretation we can taken from our data is that the valley incision under which we collected our data is most likely associated with late-stage erosion of the Colorado River and the Colorado River watershed. The mechanism of incision of incised valleys around the Colorado river is still highly debated (Spencer and Pearthree 2001, Wolkowinsky and Granger 2004), and cannot be constrained in this study.

The main contribution our research makes to the field of TCN dating and the geomorphological evolution of the Colorado Plateau is that it illustrates the proven ability to date samples at depth from muon-induced TCN production at high enough precision to reasonably determine erosion rate and age of the incision. This study has also provided a data point in a region of the Colorado Plateau that has been largely passed over for erosion rate and geomorphological changes associated with the Colorado River in favor of the Grand Canyon Province where the majority of studies take place (Darling et al., 2012; Pederson, Burnside, Shipton, & Rittenour, 2013; Pederson, Karlstrom, Sharp, & McIntosh, 2002, etc.)

6.1 Recommendations for future work

The next stages of work involve conducting further purification of samples that did not produce sufficient currents in the AMS run to yield sufficient ^{10}Be/^{9}Be ratios. We recommend increasing the size of the sample, perhaps up to 100 g to determine if purity can be improved. Additionally, we recommend that the post-tandem stripper not be used in future runs, as we

achieve samples that are free of ^{10}B at the CRISDal Laboratory, and could see an increase in precision with the removal of the stripper, allowing more counts to be delivered to the detector. As well, conducting a ^{14}C run is recommended for the remaining sample material to attempt to constrain a lower limit on irradiation age.

Of the six samples collected from the SUFCO Mine (Convulsion Canyon) incision, only three samples produced usable data to construct a depth profile across one side of the valley. To achieve a more detailed picture of the relationship between concentration of ^{10}Be atoms and depth per sample, a profile that encompasses the full range of topographic change over the incision is more useful.

Additionally, two separate samples were collected from the Dugout Mine for the express purpose of testing the quantifiable production at depths up to 300 m below the surface of the Book Cliffs. Due to the very poor quality of the material in these samples, they were not processed as part of this project, and time was allotted to sample that would more likely produce usable results. The processing method for these two samples would be the same as applied to the SUFCO samples.

Finally, further work in understanding incision on other sites in the Northern Uinta Basin region would be valuable to compare local incision rates to our study and to apply this muon-based method to a larger dataset. This could begin to build foundations for a more detailed model of how geomorphological change occurred in the northern, understudied regions of the Colorado Plateau, and the Colorado River.

7 REFERENCES

Anderson, R.S., Betancourt, J.L., Mead, J.I., Hevly, R.H., and Adam, D.P. 2000. Middle- and late-Wisconsin paleobotanic and paleoclimatic records from the southern Colorado Plateau , USA. Palaeogeography, Palaeoclimatology, Palaeoecology, **155**: 31–57. Elsevier. doi:10.1016/S0031-0182(99)00093-0.

Arvidson, R., Drozd, R.J., Hohenberg, C.M., Morgan, C.J., and Poupeau, G. 1975. Horizontal transport of the regolith, modification of features, and erosion rates on the lunar surface. The Moon, **13**: 67–79. doi:10.1007/BF00567508.

Axelrod, D.I. 1985. Rise of the grassland biome, central North America. The Botanical Review, **51**: 163–201. doi:10.1007/BF02861083.

Bird, P. 1979. Continental Delamination of the Colorado Plateau. Journal of Geophysical Research, **84**: 7561–7671.

Anderson, R.S., Betancourt, J.L., Mead, J.I., Hevly, R.H., and Adam, D.P. 2000. Middle- and late-Wisconsin paleobotanic and paleoclimatic records from the southern Colorado Plateau , USA. Palaeogeography, Palaeoclimatology, Palaeoecology, **155**: 31–57. Elsevier. doi:10.1016/S0031-0182(99)00093-0.

Blair, W.N., and Armstrong, A.K. 1979. Hualapai limestone member of the Muddy Creek Formation: the youngest deposit predating the Grand Canyon, southeastern Nevada and northwestern Arizona. U.S. Geological Survey professional paper 1111,: 14, 19 plates.

Borchers, B., Marrero, S., Balco, G., Caffee, M., Goehring, B., Lifton, N., Nishiizumi, K., Phillips, F., Schaefer, J., and Stone, J. 2016. Quaternary Geochronology Geological calibration of spallation production rates in the CRONUS- Earth project. Quaternary Geochronology, **31**: 188–198. Elsevier B.V. doi:10.1016/j.quageo.2015.01.009.

Braucher, R., and Bourle, D.L. 1998. Brazilian laterite dynamics using in situ-produced 10 Be. Earth and Planetary Science Letters, **163**: 197–205. doi:10.1016/S0012-821X(98)00187-3.

Braucher, R., Brown, E.T., Bourles, D.L., and Colin, F. 2003. In situ produced 10 Be measurements at great depths : implications for production rates by fast muons. Earth and Planetary Science Letters, **211**. doi:10.1016/S0012-821X(03)00205-X.

Brown, E.T., Bourlès, D.L., Colin, F., Raisbeck, G.M., Yiou, F., and Desgarceaux, S. 1995. Evidence for muon-induced production of10Be in near-surface rocks from the Congo. Geophysical Research Letters, **22**: 703–706. doi:10.1029/95GL00167.

Bureau of Reclamation. 2012. Colorado River Basin Water Supply and Demand Study. Colorado River Basin Water Supply and Demand Study, **acsa**.

Cook, K.L., Whipple, K.X., Heimsath, A.M., and Hanks, T.C. 2009. Rapid incision of the Colorado River in Glen Canyon – insights from channel profiles , local incision rates , and modeling of lithologic. doi:10.1002/esp.

Darling, A.L., Karlstrom, K.E., Granger, D.E., Aslan, A., Kirby, E., Ouimet, W.B., Lazear, G.D., Coblentz, D.D., and Cole, R.D. 2012. New incision rates along the Colorado River system based on cosmogenic burial dating of terraces : Implications for regional controls on Quaternary incision. : 1020–1041. doi:10.1130/GES00724.1.

Dubiel, B.R.F., Kirschbaum, M.A., Roberts, L.N.R., Mercier, T.J., and Heinrich, A. 2000. Geology and Coal Resources of the Blackhawk Formation in the Southern Wasatch Plateau , Central Utah Geologic Assessment of Coal in the Colorado Plateau : U.S. Geological Survey Professional Paper,.

Faulds, J.E., Wallace, M. a., Gonzalez, L. a., and Heizler, M.T. 2001. Depositional environment and paleogeographic implications of the late Miocene Hualapai Limestone, northwestern Arizona and southern Nevada. Colorado River origin and evolution, **12**: 81–87.

Fenton, C.R., Mark, D.F., Barfod, D.N., Niedermann, S., Goethals, M.M., and Stuart, F.M. 2013. 40Ar/39Ar dating of the SP and Bar Ten lava flows AZ, USA: Laying the foundation for the SPICE cosmogenic nuclide production-rate calibration project. Quaternary Geochronology, **18**: 158–172. Elsevier B.V. doi:10.1016/j.quageo.2013.01.007.

Garvin, C.D., Hanks, T.C., Finkel, R.C., and Heimsath, A.M. 2005. Episodic incision of the Colorado River in Glen Canyon , Utah. Earth Surface Processes and Landforms, **984**: 973–984. doi:10.1002/esp.1257.

Granger, D.E., and L. Smith, A. 2000. Dating buried sediments using radioactive decay and muogenic production of 26Al and 10Be. Nuclear Instruments and Methods in Physics Research Section B: Beam Interactions with Materials and Atoms, **172**: 822–826.

doi:10.1016/S0168-583X(00)00087-2.

Heisinger, B., Lal, D., Jull, A.J.T., Kubik, P., Ivy-ochs, S., and Knie, K. 2002a. Production of selected cosmogenic radionuclides by muons : 2 . Capture of negative muons. Earth and Planetary Science Letters, **200**: 357–369.

Heisinger, B., Lal, D., Jull, A.J.T., Kubik, P., Ivy-ochs, S., and Neumaier, S. 2002b. Production of selected cosmogenic radionuclides by muons 1 . Fast muons. Earth and Planetary Science Letters, **200**: 345–355.

Karlstrom, K.E., Crow, R., Crossey, L.J., Coblentz, D., and Van Wijk, J.W. 2008. Model for tectonically driven incision of the younger than 6 Ma Grand Canyon. Geology, **36**: 835–838. doi:10.1130/G25032A.1.

Murray, K.E., Reiners, P.W., and Thomson, S.N. 2016. Rapid Pliocene – Pleistocene erosion of the central Colorado Plateau documented by apatite thermochronology from the Henry Mountains. **44**: 483–486. doi:10.1130/G37733.1.

Pederson, J., Burnside, N., Shipton, Z., and Rittenour, T. 2013a. Rapid river incision across an inactive fault — Implications for patterns of erosion and deformation in the central Colorado Plateau. : 513–520. doi:10.1130/L282.1.

Pederson, J., Karlstrom, K., Sharp, W., and McIntosh, W. 2002a. Differential incision of the Grand Canyon related to Quaternary faulting - Constraints from U-series and Ar/Ar dating. Geology, **30**: 739–742. doi:10.1130/0091-7613(2002)030<0739:DIOTGC>2.0.CO;2.

Pederson, J.L., Hidy, A.J., Gosse, J.C., Rittenour, T.M., Pederson, J.L., Hidy, A.J., Gosse, J.C., and Tammy, M. 2013b. Plateau bull ' s-eye of incision. : 2013–2014. doi:10.1130/G34937Y.1.

Pederson, J.L., Hidy, A.J., Gosse, J.C., and Tammy, M. 2013c. Colorado River chronostratigraphy at Lee's Ferry, Arizona, and the Colorado Plateau bull's-eye of incision. : 34937. doi:10.1130/G34937Y.1.

Pederson, J.L., Mackley, R.D., and Eddleman, J.L. 2002b. Colorado Plateau uplift and erosion evaluated using GIS. GSA Today, **12**: 4–10. doi:10.1130/1052-5173(2002)012<0004:CPUAEE>2.0.CO;2.

Spencer, J.E., and Pearthree, P.A. 2001. Headward Erosion Versus Closed-basin Spillover as Alternative Causes of Neogene Capture of the Ancestral Colorado River by the Gulf of California. Colorado River origin and evolution,: 215–220.

Staiger, J., Gosse, J., Toracinta, R., Oglesby, B., Fastook, J., and Johnson, J. V. 2007. Atmospheric scaling of cosmogenic nuclide production: Climate effect. Journal of Geophysical Research: Solid Earth, **112**: 1–8. doi:10.1029/2005JB003811.

Wolkowinsky, A.J., and Granger, D.E. 2004. Early Pleistocene incision of the San Juan River, Utah, dated with 26 Al and 10 Be. Geological Society of America, **32**: 749–752. doi:10.1130/G20541.1.

9 APPENDIX A: GEOLOGIC BACKGROUND

Colorado Plateau is a thick, high-standing crustal block surrounded by deformed rock located in the southwestern region of the United States, with margins marked by volcanics and high relief. It covers an area of 225,308 km2 (140,00 mi2) and overlies portions of Utah, Arizona, Nevada, and New Mexico. It is anomalously surrounded by highly-deformed geological phenomena, including the Uinta Mountains and Rocky Mountains to the north, the Rio Grand Rift Valley to the east, the Mogollon Rim to the south, and the Basin and Range Province-Colorado Plateau Transition zone to the West. The Colorado Plateau possesses unique geophysical characteristics to other areas in the region, including relatively low heat flow and distinct gravity and magnetic signatures (Foos, 1999).

REGIONAL STRATIGRAPHY

The Colorado Plateau basement consists of Precambrian schist below shallow Cambrian to Mississippian shallow marine strata. During the Jurassic and Cretaceous Periods, the Nevadan and Sevier Orogenies were taking place to the west of the proto-Colorado Plateau, and created highlands that eroded downslope onto the plateau. Our sample material was obtained from the Blackhawk Formation embedded in the Mesaverde Group deposited concurrently with the eroding material. Consisting of a brackish-water coal facies, the Blackhawk Formation, deposited along the western inland shore of the Western Interior Seaway, is part of the Mesaverde regressive sequence that transitions from marine sand grading westward into brackish-water into fluviatile non-marine deposits (Fisher et al. 1960). This depositional strata

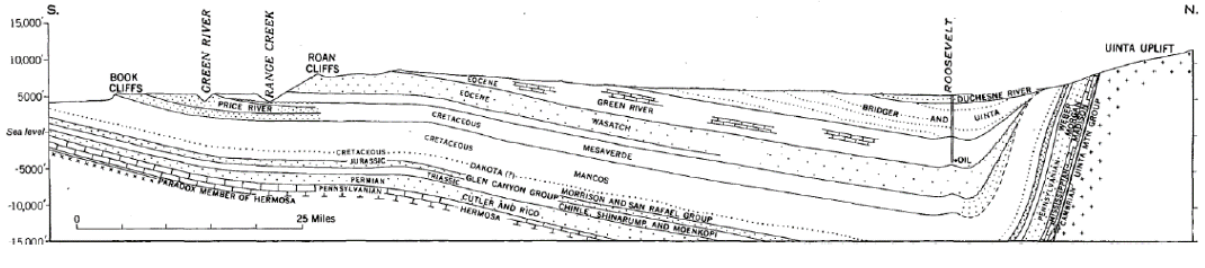

Figure 1. Graphic of the S-N cross-sectional transect from the Book Cliffs to the Uinta Uplift in the north. The formation accessed at the Sufco Mine for this study were taken from the Blackhawk Formation, part of the larger Mesaverde Group, regressive-transitional facies set from marine sand to fluviatile deposits (Modified from the American Association of Petroleum Geologists Bulletin, v. 35, 1951, fig 61).

outcrops in the Dakota and Mesaverde Group in the Grand Canyon, and the Dakota, Mesaverde, and Mancos Groups in the Book Cliffs (Hunt, 1956).

The fluvial evolution of the Colorado River is partially influenced by the Laramide Orogeny. The structural remnants of the Laramide Orogeny influenced the downslope direction, pooling, and convergence of the early Colorado River tributaries during the Late Cretaceous into the Early Tertiary. While the Colorado Plateau strata is predominantly planar with some faulting, the surrounding region underwent deformation from the Laramide Orogeny. In the Eocene, the uplifted Rocky Mountains eroded downslope onto the near sea-level plateau, burying the remnant Laramide structures.

Around 5 Ma, epeirogenic uplift originating from mantle upwelling occurred, uplifting the entire Colorado Plateau and Rocky Mountain region by 4000-6000 ft. This uplift is characterized by little surficial deformation. Precambrian basement faults underwent reactivation, facilitating the movement of the Colorado Plateau crustal block, and results in both uplift and tilting to the north (Foos, 1999). This tilting of the ground surface, in combination with the rapid uplift of the region, allowed fluvial systems in the region, including the early Colorado River, to begin rapid downslope incision to the southwest towards the Gulf of California, a flow direction which still exists today (Lucchitta, 1979, 1989). These streams, as can be observed in the Grand Canyon, cut through Cenozoic strata and Laramide structures alike.

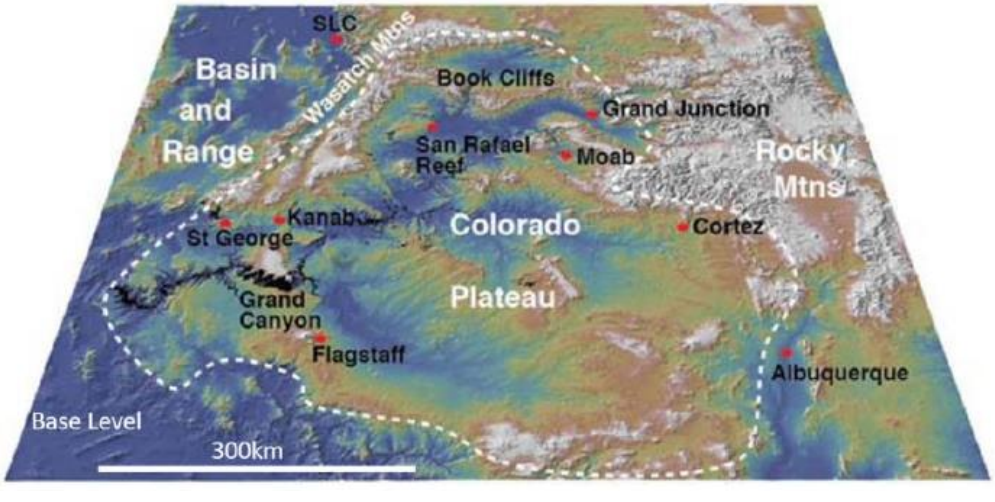

Figure 2. Topographic map of the Colorado Plateau and the surrounding regions including the Basin and Range Province and the Rocky Mountains. the study area is located in the Northeast portion of the Colorado Plateau and is identified by the arrow. The Grand Canyon is visible in the Southwestern portion of the Colorado Plateau, and represents the area where most studies on geomorphological evolution of the Colorado Plateau have occurred (Modified from Fossen, H.).

The relevancy of understanding the degree of geomorphologic evolution on the Colorado Plateau has applications to quantifying change in other heavily incised regions, both terrestrially and on a planetary scale. Prevent uplift-related incision exists in the Andes such as the San Juan River and the Central Andean Plateau (cite), where incision and uplift have occurred simultaneously over the past 9 Ma (). One of the most striking examples of large scale incision is the Valles Marineris on the Martian surface, the origin and development of which is still highly debated (Peulvast et al. 2001). By applying the known relationship between climate and tectonics identified and reinforced by terrestrial processes, including the Colorado Plateau, contribution to the study of extraterrestrial geomorphological problems can be better addressed.

On Earth, better quantification of the rate of change in geomorphological evolution of a landscape is applicable to coastal evolution, slope and soil erosion management, and hazard mitigation in well-populated areas near rivers, high-relief systems, and coasts.

TECTONISM & THE COLORADO PLATEAU

Since the Late Cretaceous Period, the Colorado Plateau has undergone several stages of tectonism, ultimately impacting the final orientation of the Plateau, fluvial flow directions, and drainage patterns seen today. Three main hypotheses exist for the stages of Colorado Plateau uplift (Humphreys 1995); flat slab subduction, crustal thickening, and anomalous mantle properties during two active stages (1) Early Cenozoic (Laramide) uplift, and (2) Middle- Late Cenozoic epeirogeny (Pederson et al., 2005).

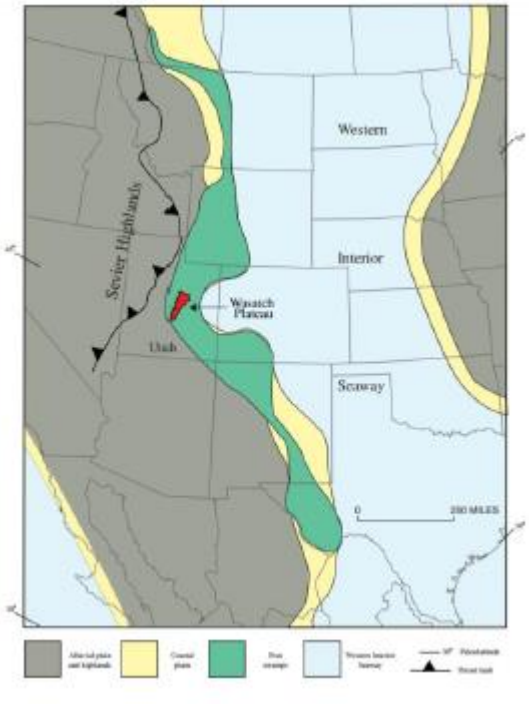

Figure 3. Diagram depicting the location of the Wasatch Plateau (which contains the Book Cliffs and our study area) along the western coast of the Western Interior Seaway that existed during the late Cretaceous throughout the western United States and Western Canada (Modified from USGS).

In the Late Cretaceous Period, the low angle subduction of the Farallon slab below the western edge of the North American plate resulted in mantle upwelling, and the formation of the Laramide Orogeny on the western flank of the Colorado Plateau (Spencer 1996). The Laramide Orogeny is responsible for uplifting of the

southern western region of the Colorado Plateau, directing plaeoflow towards the Northeast (Liu and Gurnis 2010). This uplift began to settle prior to the Oligocene, as isostatic and tectonic re-equilibration of the plateau took place. In the Miocene, uplift occurred from the northwestern regions due to the Sevier/End Laramide Orogenies. Plaeoflow through the Grand Canyon drainage system was redirected towards the southwest during this stage, and drainage patterns are theorized to be heavily influenced by paleo canyons-formed from the presence of structural features of the Laramide orogeny, some which have been buried by Neogene sediment (Spencer and Pearthree 2001). The tectonic orientation of the Colorado Plateau has re-equilibrated following the Miocene, with Colorado River draining through the Grand Canyon to the southwest, eventually flowing into the Gulf of California, in addition to lesser drainage volumes flowing off the edge flanks of the Colorado Plateau (Pederson et al. 2013b).

CLIMATE OVER THE PAST 10 MA

A record of climate change over the last 10 Ma is preserved in the strata of Book Cliffs, and can aid the interpretation of uplift and incisional histories. Globally, the Miocene was a time of increased aridity and warming of the planet (Flower and Kennett 1994, Zachos et al. 2001). On the North American continent, this warming contributed to the transition of landscapes to arid grasslands (Axelrod 1985, Smiley et al. 2017). There is no evidence of Pleistocene glaciation on the Colorado Plateau; North American glaciation contributes indirectly by influencing increased aridity in the region.

DISAGREEMENT ON CAUSE, TIMING, AND RATE OF INCISION PROCESSES

Several complexities arise when attempting to reconstruct the early incision history of the Colorado River in the Uinta Basin, mainly regarding what constitutes the starting point of Colorado Plateau incision. From work done by Lucchitta et al. (1989), the deduction of the official origin of the Colorado River is in the fluvial mouth reaching the Gulf of California, which is dated to 5.97 Ma from Spencer et al. (2001). Additionally, little previous research in the Uinta basin region exists; most research on the incision of the Colorado Plateau has been done in the Grand Canyon region owing to excellent exposure and its relatively high relief (Anderson et al. 2000, Pederson et al. 2002a, 2002b, 2013a, 2013b, 2013c, Karlstrom et al. 2008, Darling et al. 2012). This discussion consists of inconsistent erosion rates, and debates over the initiation method of erosion by the Colorado River.

The erosion rates of the Colorado River and its tributaries across the Colorado Plateau have not been consistent over time, nor are they constant across the plateau. Variation in erosion rates have been observed by numerous studies over a period of 500 ka or younger and present erosion rates between 0.072 m ka-1 (Pederson et al. 2001) and 0.7 m ka-1 (Garvin et al. 2005). Additionally, the distribution of the paleo-erosion rates of the Colorado River and its tributaries dissipates towards the edges of the plateau in a bull's eye pattern (Pederson et al., 2002). The spatial and temporal inconsistencies of the history of the Colorado River and its tributaries have presented as an issue for resolving the chronology of the geomorphological change that has occurred on the Colorado Plateau as it is associated with the relationship between uplift and erosion. The relationship between uplift and incision are further complicated by the enigmatic tectonic history of the Colorado Plateau Province. The mechanisms that caused the large-scale deformation of the Western United States during the Laramide Orogeny, while concurrently leaving the Colorado Plateau Province relatively under-deformed is believed to be attributed to mantle convection, but further research and investigation is necessary to resolve the cause (Bird 1979, Molnar et al. 1993, Zandt et al. 1995, Spencer 1996, Pederson et al. 2002b, Moucha et al. 2009, Liu and Gurnis 2010, Levander et al. 2011, Roberts et al. 2012). The effects of regional uplift on incision by the Colorado River have been discussed by Karlstrom et al. (2008) not limited to the effect of regional faulting on the flow pathways, and rate and distribution of early incision (Spencer and Pearthree 2001, Pederson et al. 2002a, 2013a).

Reconstruction of how erosion rate has changed over the last 10 Ma with consideration for tectonic influences and plateau physiography must be accounted for. The significance of Laramide paleo-canyons and their influence on the early incision history of the Colorado River has been widely debated. The debate regarding mechanisms of the Colorado River's proto-evolution is supported by two schools of thought. Lucchitta et al. (2001) argued in favour of head-ward erosion from the southern region of the plateau, moving northward into the more northerly regions of the Colorado. The other school states that top-down basin spill-over (e.g. (Pederson et al. 2002a) is the cause of initial incision. The basin spill-over theory is a much stronger case than head-ward erosion based on the spatial variation in current rates of erosion throughout the region. However, the mechanisms of initial incision and the tectonic and

physiographic influences on the early incision history of the Colorado River need to be considered in any landscape evolution model for the Colorado Plateau. The debates regarding the pattern of incision on the Colorado Plateau are currently based on evidence of (1) uplift from mantle sources, (2) denudation patterns influenced by regional topography and faulting, and (3) isostatic feedback and drainage integration owing to exhumation intensities from crustal rock variability across the Colorado Plateau. The variation in collected incision rates across the Colorado Plateau depict a variation in rates of erosion during the mid-to-late Pleistocene which form a bullseye (Pederson et al. 2013b) depicting high rates of erosion focused at the center of the Colorado Plateau that taper out towards the edges of the Colorado Plateau. Works determining the original timing of incision is currently inconclusive due to the complex tectonic history of the Colorado Plateau and the reversal of paleodrainage directions since the Late Cretaceous Period. This study agrees with work- from (Pederson et al. 2002a) in constituting the primary influence of the of remnant Laramide Miocene-aged paleo-canyons as early catalysts for plateau denudation. Known erosion rates of the Colorado River are considerably more agreeable with top-down basin spill-over versus head-ward erosion from the Southwest region of the Colorado Plateau from Lucchitta et al. (2001).

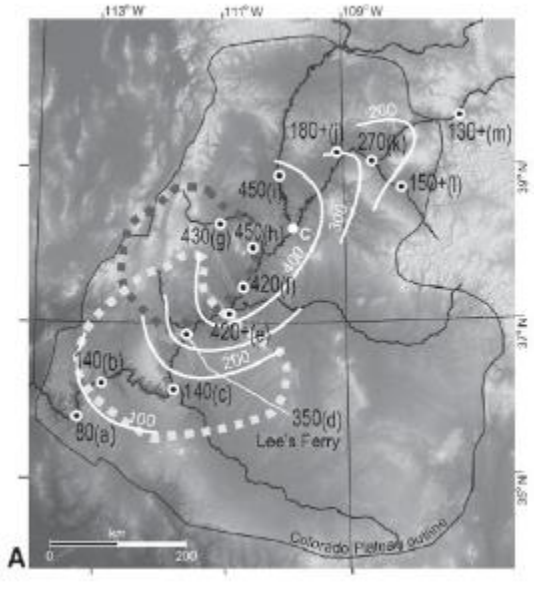

Figure 4. Figure of bullseye formation of incision rates outward from the center of the CP (Modified from Pederson 2013)

APPENDIX B: PRINCIPLES OF TERRESTRIAL IN SITU COSMOGENIC NUCLIDE (TCN) METHODS

Cosmogenic Nuclides (CN's) are formed when Cosmic Radiation (CR) interacts with atoms in exposed minerals on Earth. The commonly measured radioactive TCN's are 10Be, 14C, 26Al, and 36Cl, the common stable isotopes are the noble gases 3He and 21Ne, and many other TCN's have been measured including 7Be, 41Ca, 59Ni, depending on the mineral chemistry and the desire for a particular half-life. TCN are measured to determine a number of parameters that are important to surface processes research on Earth (D. Lal 1991, Gosse and Phillips 2001). Parameters include (i) duration of exposure to CR, (ii) duration of shielding from CR following a period of exposure ('burial dating'), and gradual (Lal and Chen 2005) or episodic (Margreth et al. 2016) erosion rate of a surface ranging from individual boulders to entire catchments. Cosmogenic nuclides have also been used on other planetary surfaces and meteorites (Gosse and Klein, 2015) including Mars (Farley et al. 2014) and the lunar surface (Arvidson et al. 1975). This thesis will explore a new approach to evaluate surface erosion by stream incision, by using the product of the interaction between secondary muons and deeply exposed minerals. This chapter will provide a brief synthesis of the physics behind the TCN method.

The primary Galactic Cosmic Radiation (GCR) consists of high energy particles (104 to 1020 eV). The majority of GCR are protons and higher mass atomic nuclei. The remaining 10% are electrons, positrons, and gamma rays (photons). GCR received by Earth originates as particles accelerated through interstellar space by supernovae explosions and magnetic fields within the Milky Way Galaxy. The supernovae produce particles with energy spectra mostly between 300 MeV – 1 GeV, but particles with energies above 1020 eV have been detected. GCR with energies of at least 500 GeV can penetrate the Earth's magnetic field.

The interaction of GCR with particles in the earth's atmosphere and lithosphere results in several processes that induces cosmic ray showers. The dominant process is spallation, with other methods including thermal neutron capture, fast muons, and slow muons. These cosmic ray showers consist of rapidly decaying leptons, hadrons and mesons that do not heavily interact with surrounding matter. Within the first 10% of the atmosphere, following the initial interaction of GCR with matter in the atmosphere, the majority of cosmic ray showers consist of secondary particles that have sufficiently small mass and cross section to bypass matter in the lower regions of the atmosphere. These secondary flux particles include neutrons, gamma rays (photons),

muons, kaons, pions, electrons, positrons, and leptons. The existence of these secondary flux particles ultimately lead to the production of cosmogenic nuclei (CN) in the atmosphere and at depth; CN can also be produced from primary cosmic radiation (PCR).

Most exposure dating studies using TCN focus on the production of the TCN induced from nucleonic spallation in shallow rock depths (<10 hg/cm-2). Neutrons are produced in the atmosphere and at surface at a greater rate than secondary particles including muons because of their larger cross-section and shorter attenuation length; these characteristics result in a high rate of interaction with matter at surface to depths of 4 m. Therefore, spallation production of TCNs constitutes 98% of production at surface down to depths of 4 m (1,000 g.cm2), with the remaining 2% attributed to less abundant muon-induced TCN production. Conversely, at depths greater than 4 m (>1,000 g cm-2), neutron-induced TCN production by spallation exponentially decreases with depth because of the neutron's larger cross-section and smaller attenuation length, and muonic production becomes the primary production mechanism. From a production ratio of muon-induced production to neutron-induced production of 1:1 at 4 m, the ratio changes to 5:1 at greater depths.

The production of cosmogenic nuclides is very different from the production of radiogenic and nucleogenic nuclides. Where radiogenic nuclides occur as the daughter product of radioactive decay, and nucleogenic nuclides are produced from the energetic particle interaction with a recently decayed daughter product, cosmogenic nuclide dating is applied to exposure history questions by utilizing the measurable accumulation, production, and/or decay of cosmogenic nuclides. To produce a cosmogenic nuclide, substantial amounts of energy is required to exceed the binding energy, a value of >3 MeV per target nucleon, to enable

production. In turn, the accumulation, production, and decay of cosmogenic nuclides is dependent on the flux of ^{10}Be that is dependent on altitude, latitude, and the strength of the

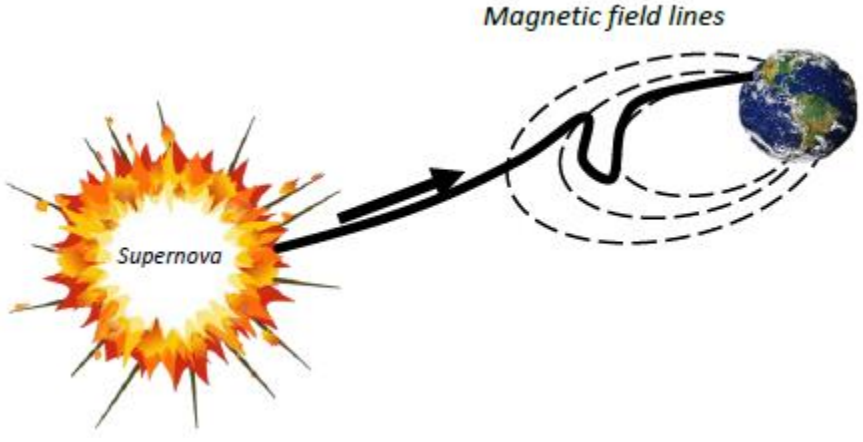

Figure 5. Transect of Galactic Cosmic Radiation (GCR) from emission from Supernova at sufficiently high energies into the Earth's magnetic field lines (Modified from Gosse & Phillips, 2001)

magnetic field. With consideration for knowledge of how production rates vary spatially and temporally across Earth's surface from differences in geomagnetic field strength and atmospheric shielding (angle of secondary CN towards target surface, assigned a value of 0-1 with one representing no shielding effects), the application of the measurement of production, accumulation and decay of cosmogenic nuclides on 10Be production in rock at the earths surface is applied a technique determining terrestrial in-situ cosmogenic nuclide (TCN) exposure history (Gosse & Klein, 2015).

CONSTANCY OF PRODUCTION RATES

Production rates of TCN vary across the surface of the earth based on four irradiation conditions: altitude, latitude, irradiation geometry, and shielding (D. Lal 1991). Latitudinal and altitudinal effects are discussed in this appendix. Irradiation geometry and shielding are not included in this appendix because of the nature of our sample site. More information of irradiation geometry and shielding can be found in Stone 2000 and Staiger et al. 2007.)

LATITUDINAL EFFECTS

Latitudinal variation is due to the distribution of the geomagnetic field lines as observed at two main latitudes; polar (>80$^{\theta}$N, S) and equatorial (0$^{\theta}$). Geomagnetic fields lines align parallel with equatorial latitudes, and perpendicularly with the polar latitudes, respectively. Though the GCR atmospheric bombardment is constant from all points of the interstellar

medium, the trajectory of GCR in sufficient proximity to the Earth's geomagnetic field will be altered according to the energy (GeV) of the incoming GCR particle. At equatorial latitudes, the parallel geomagnetic field lines prevent all but the strongest GCR to penetrate.

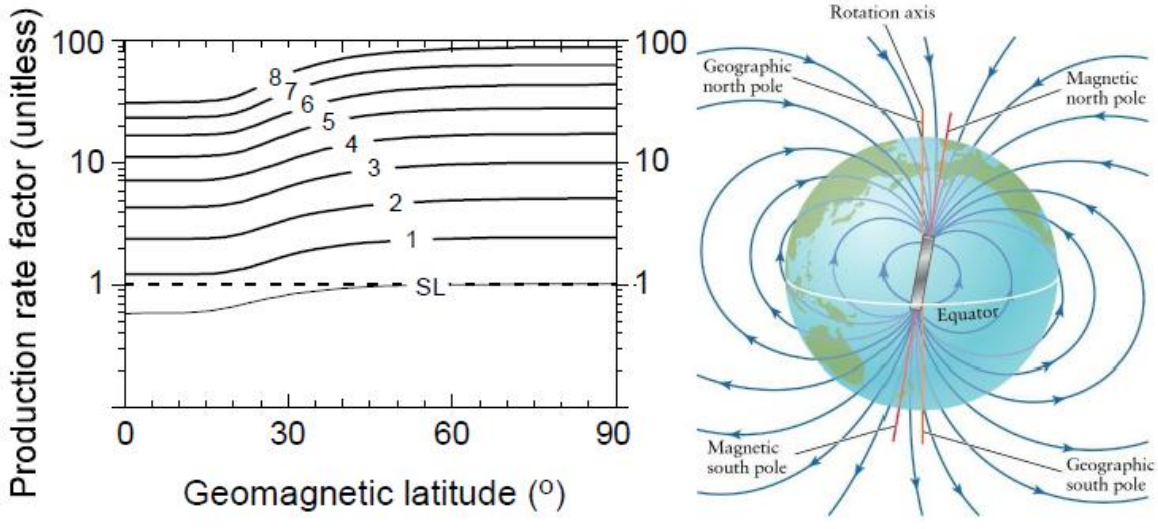

Figure 6. Figure from Lal, 1991 showing changes to production rate factor with latitude change due to threshold of bonding energy of cosmic nuclide nuclei in combination with geomagnetic cut-off rigidity as a function of dipole strength and orientation (right image from Tony Hurst, 2006).

Thus, the distribution of TCN at equatorial latitudes have the strongest incoming GCR and penetrate very deep. Conversely, at the polar latitudes, the geomagnetic field lines curve to magnetic north, and trend towards a perpendicular orientation relative to the Earth's surface. As a result, the GCR reaching the polar surface are weaker than those reaching equatorial land surface, and cannot penetrate as deep into the surface. But, not all GCR is admitted in the polar regions. Because of the minimum strength of bonding energy of GCR particles, incoming GCR that has energies at a lesser value than the bonding energy will not be able to penetrate the earths magnetic field. Logic would imply that more particles would penetrate at higher latitudes compared to equatorial latitudes, but, because of the lower minimum admittance at polar latitudes but a wider range of accepted GCR energy, in combination with the larger strength, but smaller range of accepted GCR energies at equatorial regions, the distribution of GCR between these two latitudinal extremes is relatively constant.

ALTITUDINAL EFFECTS

The effect of altitudinal variation on cosmic ray flux/production rates occurs as a function of atmospheric depth. At the top of the atmosphere, the cosmic ray flux is the highest, and decreases towards the Earth's surface as CR-matter interaction occurs more frequently as the atmosphere gets denser. As a result, the highest production rates on the surface are observed on mountains tops, while the lowest rates of production occur closest to sea level (Gosse & Klein 2015, D. Lal, 1991). the sample site at Sufco Mine in the Book Cliffs is at an elevation of 2310.16 m (7579.27 ft) above sea level. The highest regional elevation point is King's Peak 4125 m (13,534 ft), that lies north of the Book Cliffs and on the south side of the spine of the Uinta Mountains.

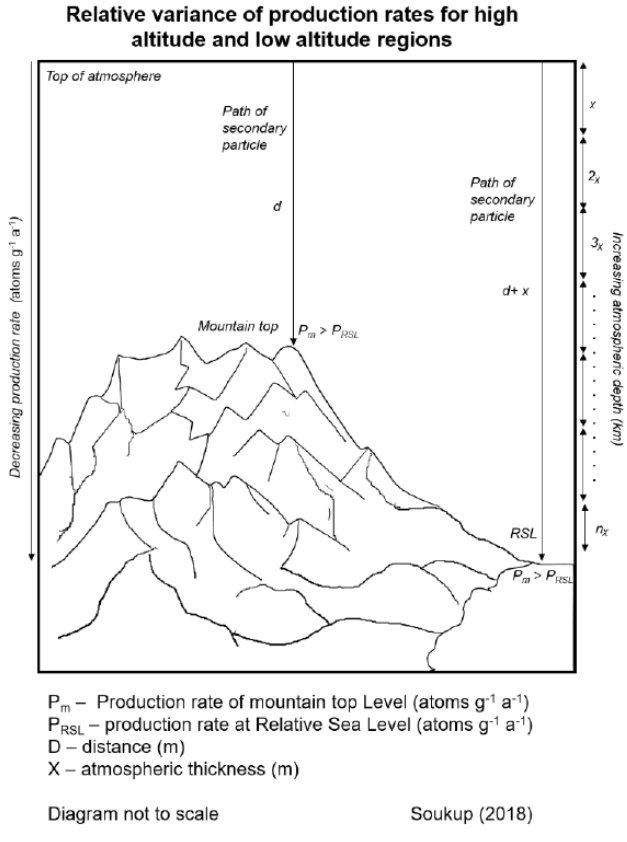

Figure 7. Image of altitudinal effect on strength of incoming secondary particles (Soukup, 2018)

THE COMBINED NULL EFFECTS OF FIELD AND SYSTEMATIC VARIATIONS

Gosse and Phillips 2001) showed by calculation that non-dipole field effects would have significant consequences on the production rates. The most recent calibration of production rates, and comparison with calendar or radiocarbon ages, reveals that indeed variations in dipole intensity and non-dipole field effects have non-trivial controls on production rates. However, because the non-dipole field effects become invariant when integrating exposures over timescales greater than about 20 ka, and because variations in paleo-intensity spanning more than 1 Ma do not contribute significant impact on the integrated production rate, for this research the impact of the geomagnetic field variations are low. However, the variation in GCR at timescales of 1 Ma may become important for this study due to the timescale over which change occurred on the Colorado River based on previous work on said incision history. Estimated to have begun

incising ~ 6 Ma (Spencer and Pearthree 2001) based on dated material from the Late Miocene Hualapai Limestone Member, the upper constraint of timing of incision for the northern region in which the study area is located is Late Miocene (6 Ma). the uppermost range that can be interpreted from 10Be concentration due to the saturation of the 10Be concentration in situ is 8 Ma; at this age, the concentration as measured against erosion rate cannot be distinguished.

APPENDIX C: CONTOUR MAP OF SUFCO MINE, UTAH

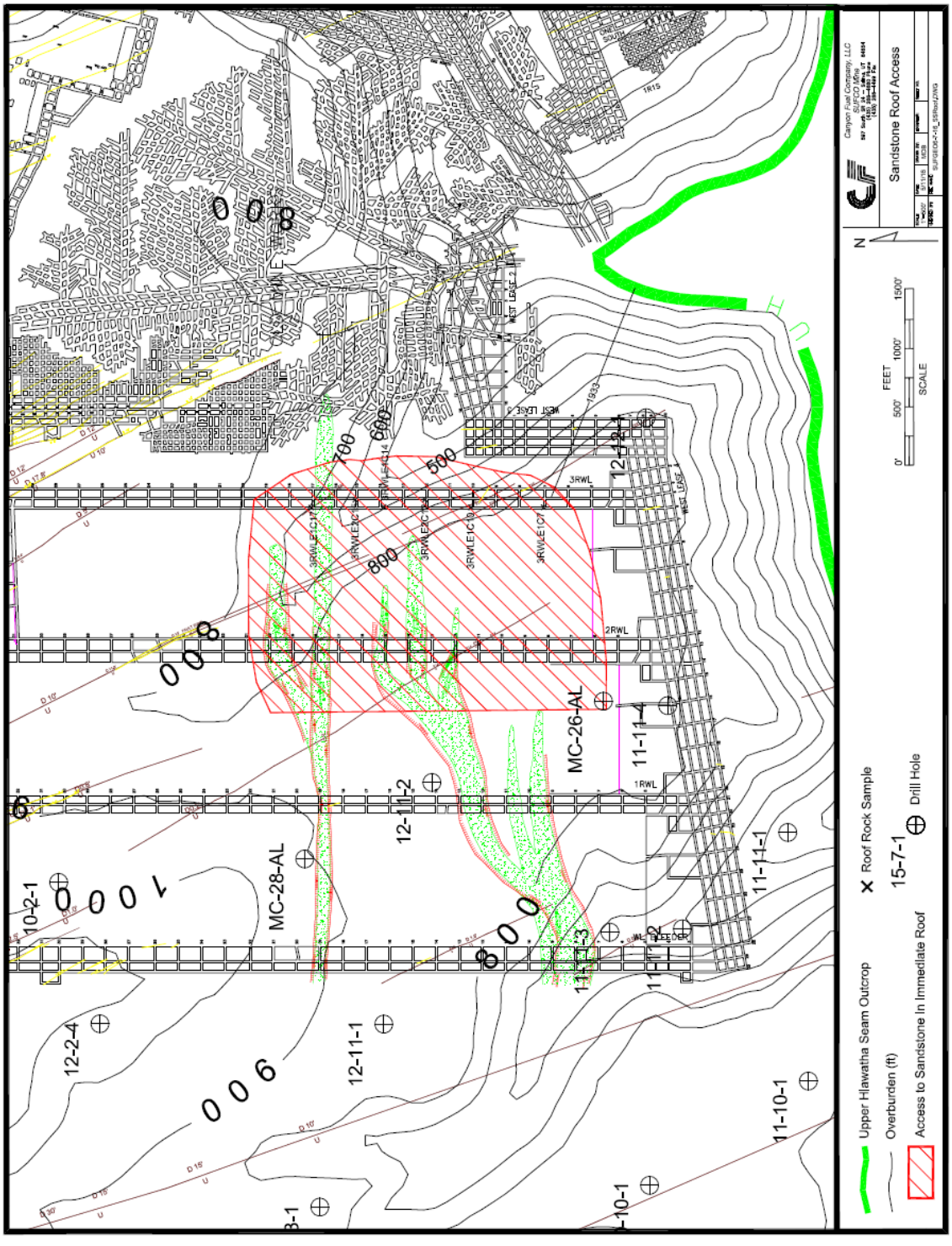

APPENDIX D: AMS DATA

SAMPLE (LLNL)	SAMPLE (CRISDAL)	CURRENT (UA)	RATIO ($^{10}BE/^{9}BE$)
BE44015	JG3524	23.178	1.48E-6
BE44016	JG3513	9.510	2.099E-6
BE44017	JG3514	14.331	1.857E-6
BE44018	JG3515	6.648	1.501E-6
BE44019	JG3516	2.637	8.895E-6
BE44020	JG3517	1.816	9.158E-6
BE44022	JG3621	9.628	3.430E-6

SAMPLE (LLNL)	SAMPLE (CRISDAL)	CURRENT (UA)	RATIO ($^{10}BE/^{9}BE$)
BE44015	JG3524	20.963	1.587E-6
BE44016	JG3513	11.337	3.51E-6
BE44017	JG3514	16.038	2.904E-6
BE44018	JG3515	7.398	2.248E-6
BE44019	JG3516	2.993	3.334E-6
BE44020	JG3517	1.970	5.066E-6
BE44022	JG3621	10.737	3.408E-6

SAMPLE (LLNL)	SAMPLE (CRISDAL)	CURRENT (UA)	RATIO ($^{10}BE/^{9}BE$)
BE44015	JG3524	20.987	7.925E-7
BE44016	JG3513	11.274	3.835E-6
BE44017	JG3514	14.877	2.236E-6
BE44018	JG3515	7.616	2.621E-6
BE44019	JG3516	2.995	3.377E-6
BE44020	JG3517	1.775	7.494E-6
BE44022	JG3621	10.510	1.582E-6

SAMPLE (LLNL)	SAMPLE (CRISDAL)	CURRENT (UA)	RATIO ($^{10}BE/^{9}BE$)
BE44015	JG3524	19.580	1.699E-7
BE44016	JG3513	10.568	2.203E-6
BE44017	JG3514	14.264	3.498E-6
BE44018	JG3515	6.877	2.902E-6
BE44019	JG3516	2.943	5.650E-6
BE44020	JG3517		
BE44022	JG3621	9.613	2.757E-6

APPENDIX E: DATA REDUCTION

KU-CRONUS CALCULATOR INPUT SPREADSHEET

FIELD ID	LATITUDE	LONGITUDE	ELEVATION	ALT TAG	THICK NESS	DENSITY	TOTAL SHIELDING	EROSION RATE	YEAR COLLECTED
(TXT)	(d.d)	(d.d)	(m)	(std)	(cm)	(g/cm3)	(unitless)	(cm/a)	2017
XX-09-XX	45.678	-70.123	1234	std	2	2.6	0.987	0.00001	
BLANK									
SUFCO-001	38.92489	-111.4206	2500	std	10	2.6	1	0.000001	2016
SUFCO-002	38.92489	-111.4206	2500	std	10	2.6	1	0.000001	2016
SUFCO-003	38.92489	-111.4206	2500	std	10	2.6	1	0.000001	2016
SUFCO-004	38.92489	-111.4206	2500	std	10	2.6	1	0.000001	2016
SUFCO-005	38.92489	-111.4206	2500	std	10	2.6	1	0.000001	2016
SUFCO-006	38.92489	-111.4206	2500	std	10	2.6	1	0.000001	2016
SUFCO-001 DUP	38.92489	-111.4206	2500	std	10	2.6	1	0.000001	2016

^{9}BE CARRIER SPREADSHEET

Qtz Mass	*Carrier Mass*	*Carrier ID*	*Carrier Conc*	*Carrier Density*	*9Be added*
(g)	(g)	(txt)	(mg/mL)	(g/mL)	(atoms 9Be)
40	0.2	Be carrier	1000	1.013	
0	0.9281	Be Carrier B31 275ug/ml sept 28, 2012	279	1.013	1.708E+19
49.9925	0.958	Be Carrier B31 275ug/ml sept 28, 2012	279	1.013	1.763E+19
50.1251	0.9305	Be Carrier B31 275ug/ml sept 28, 2012	279	1.013	1.713E+19
50.3588	0.9221	Be Carrier B31 275ug/ml sept 28, 2012	279	1.013	1.697E+19
49.9855	0.9309	Be Carrier B31 275ug/ml sept 28, 2012	279	1.013	1.713E+19
49.8968	0.9335	Be Carrier B31 275ug/ml sept 28, 2012	279	1.013	1.718E+19
50.0084	0.9241	Be Carrier B31 275ug/ml sept 28, 2012	279	1.013	1.701E+19

ACCELERATOR MASS SPECTROMETER ERROR & OTHER ERROR CALCULATIONS

ACCELERATOR MASS SPECTROMETRY

Blank ID (txt)	10Be/9Be blank boroncorr (10Be/9Be)	10Be/9Be blank error (10Be/9Be)	10Be in blank (atoms)	10Be/9Be AMS boroncorr (10Be/9Be)	1s Error (10Be/9Be)	1s Error (fraction)	10Be atoms (atoms)	10Be atoms blnk corr (Be-10 atoms)	Total Analytical Error (Be-10 atoms)	1s Total Analytical Error (fraction)	1s Total Analytical Error %
1234	**4.00E-15**	**4.00E-16**		**5.43E-13**	**9.87 E-15**						
JG3524	2.556E-16	1.58175E-16	4.367E+03								
	2.556E-16	1.582E-16	4.367E+03	1.449E-15	2.180 E-16	0.151	2.554 E+04	2.12E+04	3.92E+03	0.185	18.50%
	2.556E-16	1.582E-16	4.367E+03	1.336E-15	1.824 E-16	0.137	2.287 E+04	1.85E+04	3.36E+03	0.182	18.17%
	2.556E-16	1.582E-16	4.367E+03	1.134E-15	2.613 E-16	0.230	1.925 E+04	1.49E+04	4.03E+03	0.271	27.05%
	2.556E-16	1.582E-16	4.367E+03	2.306E-15	7.151 E-16	0.310	3.951 E+04	3.51E+04	1.12E+04	0.318	31.81%
	2.556E-16	1.582E-16	4.367E+03	3.504E-15	1.042 E-15	0.297	6.020 E+04	5.58E+04	1.68E+04	0.301	30.13%
	2.556E-16	1.582E-16	4.367E+03	1.255E-15	2.078 E-16	0.166	2.134 E+04	1.70E+04	3.55E+03	0.209	20.94%

^{10}BE CONCENTRATION SPREADSHEET

Meas Concentration	*Meas Conc Error*	*other factors*	*other factors*	*Final Concentration*	*1s Error Conc*
(Be-10 atoms/g)	(fraction)	(Be-10 atoms/g)	(fraction)	(Be-10 atoms/g)	(fraction)
4.24E+02	0.1850			**4.236E+02**	0.1850
3.69E+02	0.1817			**3.692E+02**	0.1817
2.96E+02	0.2705			**2.955E+02**	0.2705
7.03E+02	0.3181			**7.031E+02**	0.3181
1.12E+03	0.3013			**1.119E+03**	0.3013
3.39E+02	0.2094			**3.394E+02**	0.2094

FAST MUON CALCULATIONS FROM LAL ET AL., 1991

Fast Muons				*erosion rate*	*EQN (9)*	*EQN (10)*		*erosion rate*	*erosion rate*	*estimated*	*age*	*EQN(6)*
Sample ID	Concentration atoms g^{-1}	ProdRate FastMuon (atoms g^{-1} a^{-1})	m cm^{-1}	e cm a^{-1}	T_{eff} *a*	T_{eff} *a*		e cm a^{-1}	e m Ma^{-1}	me a^{-1}	*a*	*N* atoms g^{-1}
SUFCO-001	**423.6**	0.000754	0.000532	*0.0001*	1.81E+06	5.62E+05	1878	2.40E-03	24029	*5.3E-08*	*1.81E+06*	755
SUFCO-002	**369.2**	0.000964	0.000532	*0.0001*	1.81E+06	3.83E+05	1878	3.97E-03	39664	*5.3E-08*	*1.81E+06*	966
SUFCO-003	**295.5**	0.00130	0.000532	*0.0001*	1.81E+06	2.27E+05	1878	7.32E-03	73234	*5.3E-08*	*1.81E+06*	1302
SUFCO-004	**703.1**	0.00150	0.000532	*0.0001*	1.81E+06	4.69E+05	1878	3.07E-03	30685	*5.3E-08*	*1.81E+06*	1503
SUFCO-005	**1119**	0.00180	0.000532	*0.0001*	1.81E+06	6.22E+05	1878	2.08E-03	20827	*5.3E-08*	*1.81E+06*	1803
SUFCO-006												
SUFCO-001 DUP	**339.4**	0.000754	0.000532	*0.0001*	1.81E+06	4.50E+05	1878	3.23E-03	32309	*5.3E-08*	*1.81E+06*	755